

History matching for functional data and its application to tsunami warnings in the Indian Ocean

Ryuichi Kanai ^{*,†‡}
 Nicolás Hernández [§]
 Devaraj Gopinathan [¶]
 Serge Guillas ^{†‡}

September 5, 2025

Abstract

Traditional History Matching (HM) identifies implausible regions of the input parameter space by comparing scalar outputs of a computer model to observations. It offers higher computational efficiency than Bayesian calibration, making it suitable for high-dimensional problems. However, in real physical systems, outputs are often functional, such as time series or spatial fields, and conventional HM cannot fully exploit such information. We propose a novel method, Functional History Matching (FHM), which extends HM to handle functional data. FHM incorporates the Outer Product Emulator, an extension of the Gaussian Process emulator designed for time series, to enhance computational efficiency. FHM also leverages Random Projection to extract dynamic features from infinite-dimensional data, including derivatives. FHM supports uncertainty quantification essential for decision-making and naturally accommodates model discrepancies. To demonstrate its practical effectiveness, we apply FHM to a synthetic tsunami forecasting scenario in the Indian Ocean, assuming a realistic event in the Makran subduction zone. Wave elevation time series from offshore buoy data are used to predict wave elevations over the Indian coastline. Our results show that FHM significantly outperforms scalar-based HM in accuracy. FHM enables reliable forecasting from functional data within feasible computational constraints, offering a robust framework for early warning systems and beyond.

Keywords: Functional data analysis, Random projection, Model discrepancy, Functional emulator, History Matching .

*Corresponding author (Email: ryuichi.kanai.16@alumni.ucl.ac.uk)

[†]Department of Statistical Science, University College London, London, United Kingdom

[‡]Alan Turing Institute, London, United Kingdom

[§]Data Science, Statistics and Probability Centre, School of Mathematical Sciences, Queen Mary University of London, London, United Kingdom

[¶]Advanced Research Computing Centre, University College London, London, United Kingdom

1 Introduction

Tsunamis are powerful natural disasters causing widespread devastation, e.g. the 2004 Sumatran-Andaman tsunami led to more than 200,000 casualties (Lay et al. 2005) in addition to high economic losses. Such a high casualty count is partly due to the low reliability of the tsunami forecasting scheme at that time, making it difficult to determine tsunami heights immediately after earthquake event. Conventional methods have been using earthquake sources from seismological inversion to estimate tsunami wave heights. Initial estimates based on this approach can underestimate the scale of the earthquake source, leading to tsunami size estimates that are significantly lower than the actual sea surface changes (Wang et al. 2021). Additionally, the extremely complex relationship between earthquake sources and initial tsunamis implies that, even if earthquake sources are accurately estimated, it is currently impossible to precisely forecast initial tsunami scale and waveforms based solely on that information (Okal 1988, Polet & Kanamori 2000). More accurate estimation of tsunamis is achieved by directly using observations of the actual tsunami wave. For instance, Percival et al. (2014) infers the tsunamigenic earthquake source (or initial sea surface displacement) from precomputed unit sources. The unit sources are linearly superimposed using coefficients calculated by matching the cumulative wave responses to the amplitude and arrival time of the tsunami wave from buoy observations (Wang et al. 2021). However, the pre-computed tsunami database may not be accurate. For example, Gica et al. (2008), Percival et al. (2014), Tang et al. (2017) assume that a magnitude M_w 7.5 earthquake occurred in each unit to then scale linearly the resulting waves for magnitudes other than 7.5, a linear approximation that is not entirely valid. In addition, different tsunamis are generated in each unit, and this approach does not naturally reproduce initial sea surface variations within and across units. Furthermore, there is a possibility that tsunamis cannot be adequately forecasted by only using a linear combination of the tsunamis in the database, because of some dynamics in

the superposition due to rupture velocity and rise times for instance (see e.g. Gopinathan et al. (2017)). Another limitation is that this procedure may not be able to respond immediately to tsunamis caused by phenomena such as submarine landslides in regions where earthquakes do not occur.

One way to address these challenges is to use a simplified, initial tsunami wave model. Unlike the approach that assigns earthquakes to every $100 \text{ km} \times 500 \text{ km}$ grid cell and combines the resulting scenarios (Percival et al. 2014), this method produces more realistic and coherent initial waves. Our approach consists of comparing tsunami simulations to observations to identify input parameters that match observed data. Nevertheless, exhaustively searching for appropriate input values among high-dimensional input parameters through numerous simulations can be extremely costly. Additionally, since tsunami data are intrinsically continuous, processing them requires a different approach than what is used for scalar or vector discrete data.

History matching (Craig et al. 1996, Vernon et al. 2014) identifies input values that produce model outputs consistent with observations (non-implausible) or inconsistent with them (implausible). This procedure is carried out iteratively in successive waves. Additionally, history matching can account for model discrepancies, which frequently arise between simulators and observations due to lack of physics or resolution in the simulator. Moreover, while large-scale tsunami simulations are prohibitively expensive, using emulators (or surrogate statistical models) in the history matching procedure allows for efficient inference of the input parameters. This method was primarily used in the field of reservoir engineering optimisation (Kruger 1961), and it has since expanded its utility to diverse fields such as epidemiology (Andrianakis et al. 2015), climatology (Williamson et al. 2015, Salter et al. 2019, Xu et al. 2023), and astrophysics (Vernon et al. 2014). These studies have been able to target high-dimensional model outputs, albeit by focusing on reduced scalar outputs. However, the outputs of real physical systems, such as tsunami

time series data, are not represented by discrete points but appear as continuous curves. In this paper, we extend the history matching method to such curves.

Data made of continuous curves or surfaces are often referred to as functional data, initially coined by Ramsay (1982). Functional Data Analysis (FDA) deals with any type of data that can be represented as functions. The core point is considering each observation as a realization of a stochastic process taking values in a Hilbert space (Wang et al. 2016, Ramsay & Silverman 2005b) . The advantages include effectively filling missing observations acknowledging order and smoothness, obtaining information on velocity and acceleration through differentiation of continuous time series data, and avoiding the curse of dimensionality via regularization techniques. Although many techniques such as regression analysis, clustering, and principal component analysis in FDA have been studied to leverage these benefits (Wang et al. 2016), there has been no development of history matching methods in such a context.

In this study, we introduce the functional history matching (FHM) method designed to handle continuous data as model outputs for natural phenomena. As we emulate time series, we incorporate the Outer Product Emulator (OPE) as a functional emulator(Rougier 2008). The OPE method significantly reduces computational costs by decoupling input-output correlations while accounting for correlations within outputs, unlike building separate emulators independently. Furthermore, FHM involves extracting features from functional data to assess its similarities. In our approach, we use random projections to obtain a more parsimonious representation of the functions and their derivatives, while extracting essential information from the functional data through randomness (Dasgupta 2013). While the conventional history matching method for discrete data fails to leverage the inherent advantages of functional data, our approach builds on these benefits to reduce uncertainty more effectively, providing more accurate estimates and forecasts.

In this paper, Section 2 provides a detailed explanation of the FHM method that we have developed. In Section 3, we apply FHM to hypothetical tsunami scenarios in the Indian Ocean, thereby proving the validity of our approach. Section 4 summarizes the conclusions obtained from this new method.

2 Methods and Data

2.1 History Matching for Discrete Data

The observed data \mathbf{z} are assumed to be the sum of the true values \mathbf{y} , and observational errors $\boldsymbol{\phi}$:

$$\mathbf{z} = \mathbf{y} + \boldsymbol{\phi}. \quad (1)$$

We use a simulator model $f(\cdot)$ to approximate \mathbf{y} . The model discrepancy, $\boldsymbol{\delta}$, represents the gap between the simulation and the true physical system:

$$\mathbf{y} = f(\boldsymbol{\theta}) + \boldsymbol{\delta}. \quad (2)$$

However, simulation models $f(\cdot)$ are often computationally expensive, which limits the number of simulations that can be performed. To mitigate this issue, an emulator $g_{emu}(\cdot)$ is constructed using a limited set of simulation results. Acting as a surrogate model for $f(\cdot)$, this emulator also incorporates the (often small) code uncertainty $\eta(\cdot)$ (O’Hagan 2006). Using (1) and (2) we get:

$$\mathbf{z} = \mathbb{E} [f_{emu}(\boldsymbol{\theta})] + \eta(\boldsymbol{\theta}) + \boldsymbol{\delta} + \boldsymbol{\phi}. \quad (3)$$

History matching does not seek a set of values of $\boldsymbol{\theta}$ that best reproduces the observed data, unlike calibration (Kennedy & O’Hagan 2001). Instead, it aims to identify and exclude implausible parameter values, leaving what it is called the the Not-Ruled-Out-Yet (NROY) subspace, $\boldsymbol{\Theta}_n$, possibly refined over n iterations:

$$\boldsymbol{\Theta}_n \subset \boldsymbol{\Theta}_{n-1} \subset \cdots \subset \boldsymbol{\Theta}_1 \subset \boldsymbol{\Theta}. \quad (4)$$

A metric is used to identify the NROY at each iteration. The implausibility measure is used to assess whether a given set of input parameters is likely to produce model outputs inconsistent with observed data. Essentially, it quantifies the “distance” between the model’s predictions (given a specific set of input parameters) and the actual observations, taking into account various sources of uncertainty in (3):

$$I(\boldsymbol{\theta}) = \frac{|\mathbf{z} - \mathbb{E}[f_{emu}(\boldsymbol{\theta})]|}{\{Var(\mathbf{z} - \mathbb{E}[f_{emu}(\boldsymbol{\theta})])\}^{1/2}}. \quad (5)$$

This expression can also be rewritten using the variances of the three sources of errors:

$$I(\boldsymbol{\theta}) = \frac{|\mathbf{z} - \mathbb{E}[f_{emu}(\boldsymbol{\theta})]|}{\{Var(\boldsymbol{\phi}) + Var(\boldsymbol{\delta}) + Var(\eta(\boldsymbol{\theta}))\}^{1/2}}. \quad (6)$$

The implausibility measure $I(\boldsymbol{\theta})$, as shown in Eq.(6) is defined as the ratio of the discrepancy to total uncertainty. Assuming that uncertainties arising from observational error, model discrepancy, and emulator uncertainty are independent (Williamson et al. 2017), the denominator is expressed as the sum of their variances. If $I(\boldsymbol{\theta})$ exceeds a given threshold, the parameter value is deemed implausible. This approach allows parameter values to remain in the NROY subspace under conditions of high uncertainty, even when the emulator’s output deviates from observed data. In such cases, the large uncertainty increases the denominator in Eq. (6), resulting in a lower implausibility value. It highlights the importance of properly assessing uncertainty.

2.2 Functional Emulator

While simulations typically involve solving deterministic equations through numerical computations, emulation uses fast probabilistic estimates based on multiple simulation results to predict outcomes for new input values, generally approximated via the posterior mean. While Gaussian process regression is commonly used in history matching as a surrogate model to perform emulations from a discrete data simulation ensemble, we employ the OPE method developed by

Rougier (2008) for functional data, due to its ability to handle high-dimensional and continuous data (including tsunami time series as done in Guillas et al. (2018)). The OPE is a versatile emulator that models simulation outputs by combining information from both input parameters and output indices, making it more efficient and informative than traditional Gaussian process regression models used for discrete data.

In OPE, the i -th output of the simulation, $f_i(\boldsymbol{\theta})$, is represented by:

$$f_i(\boldsymbol{\theta}) = \sum_{j=1}^v \beta_j g_j(\boldsymbol{\theta}, t_i) + \varepsilon(\boldsymbol{\theta}, t_i), \quad (7)$$

where $\boldsymbol{\theta} \in \boldsymbol{\Theta}$, g_j is a regressor on $\boldsymbol{\Theta} \times \mathbf{T}$, β_j are unknown coefficients, and ε is a residual stochastic process modeled as a Gaussian Process. The OPE framework includes the following key properties that make it efficient for functional data emulation:

1. **Invariant Output Index Set:** The output index set $\mathbf{t} = \{t_1, t_2, \dots, t_q\}$ remains invariant with respect to the input values $\boldsymbol{\theta} = \{\theta_1, \theta_2, \dots, \theta_p\}$.
2. **Separable Residual Covariance:** The residual covariance function is separable between inputs $\boldsymbol{\theta}$ and outputs \mathbf{t} , which allows for computational efficiency and is defined by:

$$\kappa_{\lambda}(\boldsymbol{\theta}, \mathbf{t}, \boldsymbol{\theta}', \mathbf{t}') = \kappa_{\lambda_{\theta}}^{\theta}(\boldsymbol{\theta}, \boldsymbol{\theta}') \times \kappa_{\lambda_t}^t(\mathbf{t}, \mathbf{t}'). \quad (8)$$

In this work, we adopt the following forms for the individual components:

$$\kappa_{\lambda_{\theta}}^{\theta}(\boldsymbol{\theta}, \boldsymbol{\theta}') = \prod_{j_{\theta}}^p \exp \left[- \left(\frac{|\theta_{j_{\theta}} - \theta'_{j_{\theta}}|}{\lambda_{j_{\theta}}} \right)^{3/2} \right], \quad (9)$$

$$\kappa_{\lambda_t}^t(\mathbf{t}, \mathbf{t}') = \exp \left[- \left(\frac{|\mathbf{t} - \mathbf{t}'|}{\lambda_t} \right)^{3/2} \right]. \quad (10)$$

This separability assumes that the residuals, ε , can be expressed as independent stochastic processes over $\boldsymbol{\theta}$ and \mathbf{t} , facilitating simplified covariance estimation: $\varepsilon(\boldsymbol{\theta}, t_i) = \varepsilon^{\theta}(\boldsymbol{\theta}) \times \varepsilon^t(t_i)$ where $\varepsilon^{\theta}(\cdot) \perp \varepsilon^t(\cdot) | \tau$.

The hyper-parameters λ_{j_θ} and λ_t represent the correlation length for the inputs θ_{j_θ} and output index t , respectively, and the exponent of $\frac{3}{2}$ is chosen to ensure that the covariance function is adequately smooth without being overly so (Sarri et al. 2012, Guillas et al. 2018).

3. **Outer Product Regressors:** The regressors are constructed as the outer product of input and output regressors. Let $\{g_{j_\theta}^\theta\}_{j_\theta=1}^{\nu_\theta}$ denote the set of input-side basis functions and $\{g_{j_t}^t\}_{j_t=1}^{\nu_t}$ the set of output-side basis functions. Specifically, each function g_j in Eq. (7) can be represented by:

$$g_j(\boldsymbol{\theta}, t) = g_{j_\theta}^\theta(\boldsymbol{\theta}) \otimes g_{j_t}^t(t), \quad (11)$$

where $j = \{1, \dots, \nu\}$ and $\nu = \nu_\theta \times \nu_t$. Following (Guillas et al. 2018), for input parameter regressors, g^θ , we consider Legendre polynomials up to the second degree, whereas for the output regressor, g^t , a Fourier series up to the second order is used. This reflects the periodic nature of the T tsunami time series data, see Rougier et al. (2009), Sarri et al. (2012) for further details.

In Bayesian inference for OPE, we utilize the Normal-Inverse-Gamma (NIG) framework, which efficiently computes posterior distributions:

$$\boldsymbol{\beta} \mid (\tau, B) \sim N_v(\boldsymbol{m}, \tau V), \quad (12)$$

$$\varepsilon(\cdot) \mid (\tau, B) \sim \text{GP}(0, \tau \kappa_\lambda(\cdot)), \quad (13)$$

$$\tau \mid B \sim \text{IG}(a, d), \quad (14)$$

where the set of hyperparameters $B = \{\boldsymbol{m}, V, a, d, \kappa_\lambda(\cdot)\}$ consists of the mean vector \boldsymbol{m} and covariance matrix V for the multivariate normal distribution of regression coefficients $\boldsymbol{\beta}$, the variance inflation factor τ , and the correlation length λ that characterizes the covariance function $\kappa_\lambda(\cdot)$ for residuals, defined on $(\boldsymbol{\Theta} \times \mathbf{T})^2$. IG represents the inverse gamma distribution, where a stands for

the shape and d indicates the scale, respectively. This structure significantly reduces computational costs by allowing the use of conjugate priors, avoiding MCMC sampling.

To construct an emulator, an ensemble derived from simulation results is required. A known rule of thumb is $N = 10 \times P$, where N is the required number of simulations and P is the number of parameters (Loeppky et al. 2009). Although this rule suggests that 50 simulations are sufficient for five parameters, we conservatively use 100 simulations to ensure robustness. To conduct these simulations, input parameter values are randomly sampled from an n -dimensional parameter space using Latin hypercube sampling (McKay et al. 1979, Loh 1996). The sampling is designed to cover a broad parameter space in order to include potential parameter values that can reproduce the observed data. This broad range incorporates prior knowledge and contributes to effective model construction.

2.3 Distance evaluation via random projections

In the classical history matching approach, the computation of implausibility involves calculating the distance between observed values and emulator outputs, often using the Euclidean distance. However, since our observed data and emulator outputs are functions, it is crucial to consider an appropriate metric. Although similarity in functional spaces can be assessed using various metrics such as the L^p norms, particularly L_1 , L_2 and L_∞ , these do not account for phase variation in the functions (curves), which is a critical feature our model must capture (Marron et al. 2015).

In practice, dealing with functional data often requires the use of dimension reduction techniques. A common strategy is to map the observations onto a lower-dimensional subspace, which retains most of the data's variability. One of the most popular techniques is functional principal components analysis (FPCA) (Ramsay & Silverman 2005a). However, FPCA can be computationally expensive and there is no guarantee that the pairwise distances in the original space are

preserved after the projection in the lower dimensional subspace (Biau et al. 2008).

In this paper, we consider random projections for functional data, which offer an alternative and much more efficient method for dimension reduction, (Vempala 2005, Cuesta-Albertos, del Barrio, Fraiman & Matrán 2007). This projection method relies on the Johnson-Lindenstrauss lemma (William & Lindenstrauss 1984), which gives some general conditions to approximately preserve pairwise distances in the projection space with high probability. Specifically, it states that any set of n points in a Euclidean space, can be projected into a lower-dimensional Euclidean space of dimension $O(\log n/\varepsilon^2)$ preserving the pairwise distances within a specified relative approximation error $\varepsilon \in (0, 1)$.

We implement the random projection method in one dimensional functional space \mathcal{H} , as follows:

$$\langle f(t), h(t) \rangle = \int f(t)h(t)dt \approx \sum_i f(t_i)h(t_i)\Delta_{t_i}, \quad (15)$$

where $f(t)$ represents a functional datum and the function $h(t)$ denotes a random element in the functional space. Among various stochastic processes that can be employed as random functions in random projection procedures, we have chosen the Wiener process, which is the most fundamental form.

Once the functional data are projected onto a random direction given by $h(t)$, the distribution of the emulated curves can be characterized in the projection space. This is underpinned by the generalization of the Cramér–Wold theorem, see Cuesta-Albertos, Fraiman & Ransford (2007). According to this theoretical result, under suitable conditions, the distribution of a sample of elements in a separable infinite-dimensional space (as \mathcal{H}) can be characterized in a one-dimensional projection space provided that the direction of the projection is chosen randomly. These conditions include that the original distribution must have sufficiently well-behaved (i.e., finite and not too rapidly growing) moments, and that the random directions used for projection are selected

according to a non-degenerate Gaussian distribution—ensuring that enough meaningful projection information is captured. Under these assumptions, it is guaranteed that the full distribution can be recovered from its one-dimensional projections. The use of a randomly chosen projection direction is motivated by the computational challenges of high- or infinite-dimensional spaces, where traditional deterministic approaches such as PCA or FPCA may not be practical. Random projections offer a stochastic yet efficient alternative, leveraging variability to reduce complexity and improve tractability.

In the same vein, there is substantial research, such as Cuesta-Albertos & Nieto-Reyes (2008) and Nieto-Reyes & Battey (2016), which utilizes random projection techniques in infinite-dimensional spaces to compute depth measures. These are well-established metrics in FDA that impose a center-outward ordering on a functional data set. The implausibility measure has a similar purpose: to order functional outputs, with the ultimate goal of retaining input parameters that generate curves closely resembling the observations. Although a single randomly chosen projection direction is sufficient to characterize the distribution of the functional data, the literature suggests repeating the projection procedure to obtain more robust results (Cuesta-Albertos & Nieto-Reyes 2008, Cuesta-Albertos et al. 2006). In this case, we consider 1000 projections, and in the supplementary material (Section 3) we discuss this topic as well as the different random processes that can be considered for projecting the functional data.

2.4 Implausibility Threshold and Uncertainty Evaluation

In history matching, the evaluation of implausibility relies on Pukelsheim’s 3-sigma rule (Pukelsheim 1994). Based on this rule, observations X that deviate more than three standard deviations, σ , from the mean value, μ , are interpreted as extremely rare events. Consequently, parameter values that generate such a mean value are considered implausible. Conversely, parameter values that

yield implausibility less than 3σ are categorized as NROY (Andrianakis et al. 2015, Williamson et al. 2017). One of the assumptions underlying the 3-sigma rule is that the distribution of estimated values obtained from an emulator at fixed parameter values is unimodal. However, in our FHM approach, this condition may not always be satisfied. Hence, we use Chebyshev’s inequality, $P(|X - \mu| \geq k\sigma) \leq \frac{1}{k^2}$, as a more general bound when the emulator outputs at fixed parameters do not exhibit unimodality. In this case, with $k = 5$, the probability that the absolute difference between the observed values and the expected values exceeds 5σ is at most 4%. Therefore, we consider it reasonable to use 5 as the threshold.

The calculation of implausibility requires evaluating uncertainties, as shown in Equation 6. There are three primary sources of uncertainty: i) uncertainty due to observational errors; ii) uncertainty due to model discrepancies; and iii) uncertainty originating from emulators. Firstly, observational error is particularly difficult to estimate due to limitations of the gauge devices used. Secondly, model discrepancy is defined as the difference between the simulation outputs and the true system output (Kennedy & O’Hagan 2001, Goldstein & Rougier 2009). Thirdly, emulator uncertainty can be quantified via the OPE, as explained in the supplementary material. Consequently, decisions regarding model discrepancies and observational uncertainties are sometimes based on expert judgment or exploratory methods, rather than on formal mathematical derivation (Johnson et al. 2020, Ferreira et al. 2020).

Considering that the same buoy is used to collect the data at fixed observation points, we assume that the uncertainties due to model discrepancy and observational error are fixed values. Initially, we conservatively assume that 5% of the parameter space is not considered implausible, given our reliance on highly accurate tsunami simulations. Under this assumption, an intuitive approach is to incrementally increase the estimated uncertainty values, starting from zero (e.g., by increments of 0.001), until only 5% of the emulated curves are classified as non-implausible. However, this

Algorithm 1 Uncertainty evaluation algorithm

- 1: USE \tilde{g}_{worst} for projected $g_{worst}(t)$ {The worst-case scenario}
 - 2: USE \tilde{g}_{emu_i} for projected $g_{emu_i}(t)$ ($i = 1, \dots, n$) {The i th emulated curve}
 - 3: $dist_i = |\tilde{g}_{worst} - \tilde{g}_{emu_i}|$
 - 4: $Dist = \{dist_1, \dots, dist_n\}$
 - 5: Randomly divide $Dist$ into the same size k folds, $Dist^1, Dist^2, \dots, Dist^k$
 - 6: **for** j from 1 to k **do**
 - 7: $Dist^{-j} = Dist^1 \cup \dots \cup Dist^{j-1} \cup Dist^{j+1} \cup \dots \cup Dist^k$ {Except for $Dist^j$ }
 - 8: $a = 0$ {Potential uncertainty}
 - 9: $b = 0.05 * \frac{n(k-1)}{k}$
 - 10: USE EU_l for l th curve Emulation Uncertainty in $Dist^{-j}$ ($l = 1, \dots, \frac{n(k-1)}{k}$)
 - 11: USE U_l for l th curve Uncertainty in $Dist^{-j}$
 - 12: **repeat**
 - 13: $a = a + \delta$ { δ is small amount}
 - 14: $U_l = EU_l + a$ for all l
 - 15: Compute implausibility I_l for all element in $Dist^{-j}$
 - 16: **until** The number of elements in $NROY = b$.
 - 17: $a_j = a$
 - 18: **end for**
 - 19: Estimated uncertainty = $\frac{\sum_j^k a_j}{k}$
 - 20: **return** Estimated uncertainty
-

approach may result in the uncertainty estimates being overly tuned to the emulator outputs at the observation sites, potentially compromising the generalizability of the model. To enhance the robustness of forecasts for Mumbai, we employ a k-fold cross-validation approach to mitigate this issue. The detailed procedure is described in Algorithm 1.

2.5 History Matching for Functional Data

FHM begins by converting the observed tsunami time series data into functional forms via a basis expansion. In this case, we use a system of B-spline basis functions (see Ramsay & Silverman (2005a) for further discussion). These functional observations are later used to assess the similarity between the JAGURS tsunami simulator outputs and real-world data. To construct a functional emulator that can reproduce the model behavior across the parameter space, we first perform multiple simulations using the JAGURS tsunami model. The input parameter values for these simulations are generated using Latin hypercube sampling. The resulting outputs are then used to train the emulator based on the OPE framework. Then, both the emulated outputs and the observed data are projected onto a one-dimensional space via random projection, where the projection function $h(t)$ is drawn from a Wiener process \mathcal{W}_s . Subsequently, the implausibility index is computed by incorporating two types of uncertainty: one derived from the emulator, and the other estimated through a cross-validation-like approach that accounts for observational error and model discrepancy. Thus, the NROY parameter subspace can be determined, providing a focused domain for tsunami height forecasting and inverse estimation. A conceptual diagram of the overall process is shown in Figure 1.

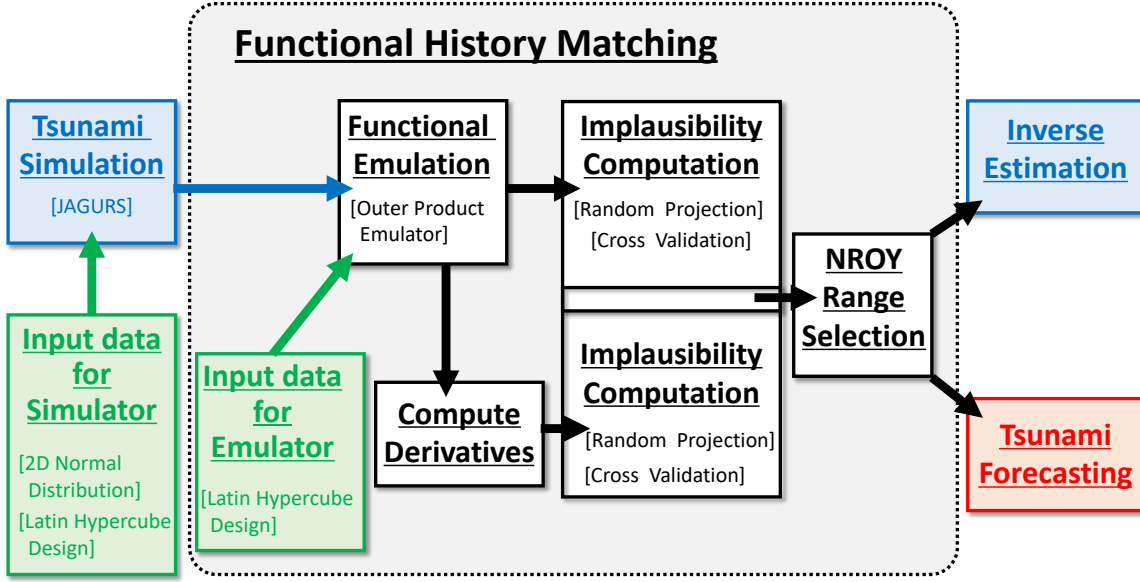


Figure 1: Comprehensive view of Function History Matching and a conceptual illustration of its use in a tsunami case in Section 3.

3 Case of Study: Mumbai coast Tsunami

The FHM framework is designed as a general approach for constraining the parameter space of complex simulators using functional data, and is therefore applicable to a wide range of systems. We present here a concrete coastal-hazard scenario. Selecting a single, data-rich example allows us to demonstrate each step: design of experiments, emulator construction, implausibility screening, and probabilistic inference, in a setting that is both reproducible and complex, which highlights the strengths of the method. While the specific modelling choices, such as the simulator, output quantities, and uncertainty specifications, are tailored to this application, the underlying logic of FHM remains unchanged and can be readily adapted to a broad class of problems.

3.1 Tsunami Simulation and Data

For the Indian Ocean tsunami simulations, we use JAGURS, an open-source simulator that has been widely applied to marine hazard modeling (Baba et al. 2015, 2017) including a recent multi-level emulation (Ehara et al. 2023). As a benchmark scenario, we adopt a hypothetical worst-case tsunami in the Makran Subduction Zone (MSZ), based on a previous study that performed one million emulator-based predictions in the region (Gopinathan et al. 2021). For observational comparison, we analyze simulated waveforms at locations corresponding to NOAA’s Deep-ocean Assessment and Reporting of Tsunamis (DART ®) stations (Gonzalez et al. 1998), specifically at the sites of DART location IDs: 23228, 23226, 23225, and 23011 (<https://www.ndbc.noaa.gov>). In addition, we include one virtual observation point in the central Indian Ocean to assess the influence of alternative observation locations, and four virtual points near the Mumbai coastline, as shown in Figure 2. Specifically, a point placed opposite the DART buoys relative to the source region is employed to investigate its impact on FHM performance (See Supplementary Material, Section 7 for further implementation details).

3.2 Experimental setting

As a case study, we present a tsunami forecasting scenario for the Mumbai coast, assuming a worst-case event occurs off the Makran coast at 10:00 AM (Gopinathan et al. 2021). As shown in Figure 2, the tsunami reached the four DART observation points (marked with red diamonds) within approximately 40 to 90 minutes, and took over 270 minutes to reach the four Mumbai observation points (marked with blue circles). In this study, the initial tsunami is modeled using a Gaussian profile for both the rising and falling phases. The tsunami shape is parameterized by five variables: θ_1 (the longitude) and θ_2 (the latitude) of the midpoint between the rise peak and fall trough; θ_3 and θ_4 , the standard deviations of the two-dimensional Gaussian in the longitudinal

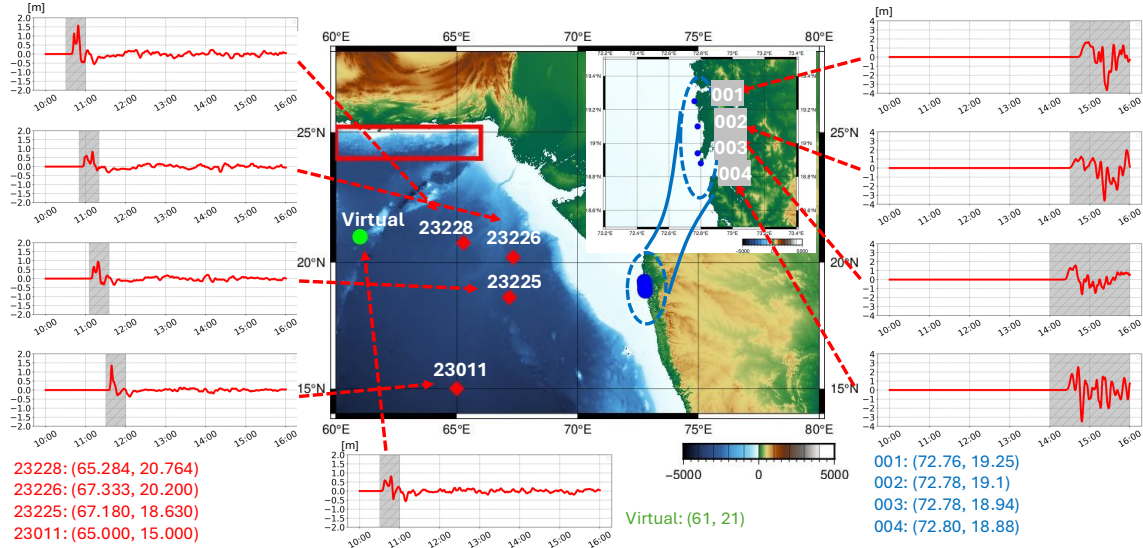


Figure 2: The worst-case tsunami time series (—) at locations of DART observation points (◆), one virtual observation point (●), and Mumbai observation points (●). The rectangular region outlined in red indicates the potential area for the midpoint (θ_1 and θ_2) between the tsunami peak and bottom in wave 1. The tsunami time series data, based on the worst-case scenario, are plotted for each point. The heights of the tsunamis are expressed in meters.

and latitudinal directions (assumed uncorrelated); and θ_5 the maximum height in meters. The distance between the peak and trough is fixed at seven times the latitudinal standard deviation θ_4 , reflecting the assumption that the tsunami source along the Makran Trench is elongated in the longitudinal direction. The parameter ranges are: $\theta_1 \in [60, 66]$, $\theta_2 \in [24, 25.2]$, $\theta_3 \in [0.5, 1.5]$, $\theta_4 \in [0.1, 0.2]$, and $\theta_5 \in [4, 12]$. Since locations are often unclear in real events, we allow θ_1 and θ_2 to vary across a broad spatial region, shown as the red rectangle in Figure 2. Within the full five-dimensional parameter space defined earlier, we draw 100 parameter sets using Latin hypercube sampling and simulate the corresponding tsunami waveforms using the JAGURS model.

3.3 Distance Evaluation

To evaluate the similarity between emulated and observed functional outputs, we project each curve from infinite-dimensional functional space to one-dimensional space using random projection. The random projection is constructed using functions sampled from a Wiener process \mathcal{W}_s , which is computationally efficient and straightforward to implement. The time scale of the Wiener process is aligned with the temporal resolution used in the tsunami simulations. Because each projection direction is random, the inner product between the projected curves varies depending on the realization. To ensure that the resulting distance measure is stable and conservative in the sense of convergence reliability, we compute the average of 1,000 inner products, each based on a different random direction sampled from the Wiener process. As demonstrated in the supplementary material (Figure S6), this ensemble-averaged projection converges well and provides a robust basis for comparing curves.

This distance evaluation plays a key role in the computation of the implausibility index, which underpins the selection of the NROY parameter subspace. If the emulator has high uncertainty, implausibility tends to be low everywhere, making it difficult to discard implausible regions. Conversely, if emulator uncertainty is moderate but the predicted curves deviate substantially from the observations, nearly all parameter combinations may be ruled out. In such cases, it is necessary to revisit model assumptions or adjust the uncertainty specification. A detailed explanation of how the implausibility is computed, including the treatment of uncertainty and the structure of the NROY space, is provided in the supplementary material.

3.4 Estimation at Observation Points and Implausibility Analysis

FHM is conducted to predict the tsunami under a worst-case scenario. The panel (a) in Figure 3 illustrates the amplitude range (upper and lower bounds) of the tsunami at DART 23228, obtained

through one million functional emulations using training data generated from initial tsunami parameters sampled by Latin hypercube design. Panel (b) shows the result of applying FHM to the original tsunami time series. Parameter sets classified as non-implausible are selected based on the implausibility index. While this approach effectively retains curves that closely match the amplitude and overall shape, it may still admit curves with phase misalignments, as evident in the panel. To address such phase-related discrepancies, we extend the FHM procedure by also applying it to the differentiated tsunami time series. Only those parameter sets that yield non-implausible results for both the original and differentiated curves are retained. This additional filtering helps to exclude curves with mismatched peak or trough positions as shown in panel (c). Results for additional observation points and the second wave (Wave 2) are provided in the supplementary material.

Figure 4 presents the highest implausibility distribution in wave 1 derived from the five-dimensional input parameter space, projected into two dimensions for visualization purposes. Here, the highest implausibility value is computed by applying the method to both the tsunami time series data and its derivative at all observation points. This figure demonstrates the success-

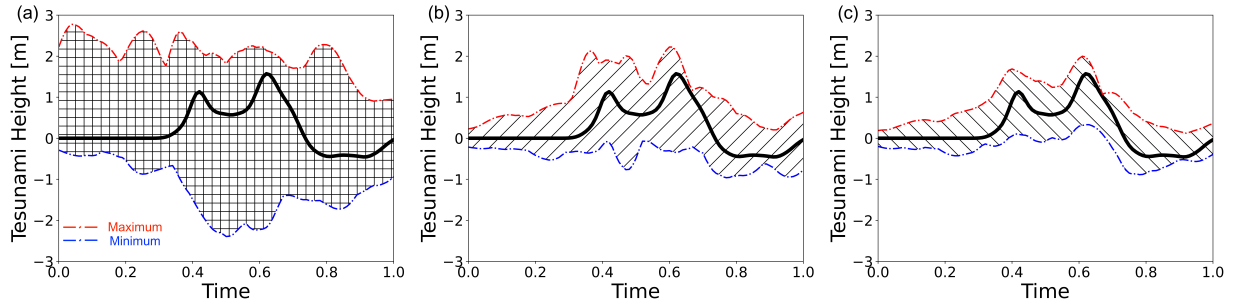


Figure 3: Emulation and FHM results at the DART23228 in wave 1. The maximum and minimum values of emulation curves are plotted. The horizontal axis is time scaled to $[0, 1]$. Panel (a): 1 million emulation output. Panel (b): FHM result with tsunami time series data (49,992 curves). Panel (c): FHM results with tsunami time series data and its derivative (18,585 curves).

ful computation of implausibility using our proposed functional history matching method. The validity of this implausibility will be discussed in the following sections.

Using the implausibility values illustrated in Figure 4, the NROY parameter subspace for wave 1 is determined. In Figure 5, the violin plot illustrates the NROY region in wave 1 within each parameter's upper and lower bounds. The figure clearly demonstrates a significant reduction in the parameters' ranges for longitude and latitude, whereas the ranges for S_{xx} , S_{yy} , and tsunami height show a minimal reduction. This suggests that our constraints for S_{xx} and S_{yy} in wave 1, based on the assumption that tsunamis occur along the trench off the Makran coast, are appropriate. We note that wave 1 is insufficient to constrain tsunami height, necessitating a second wave

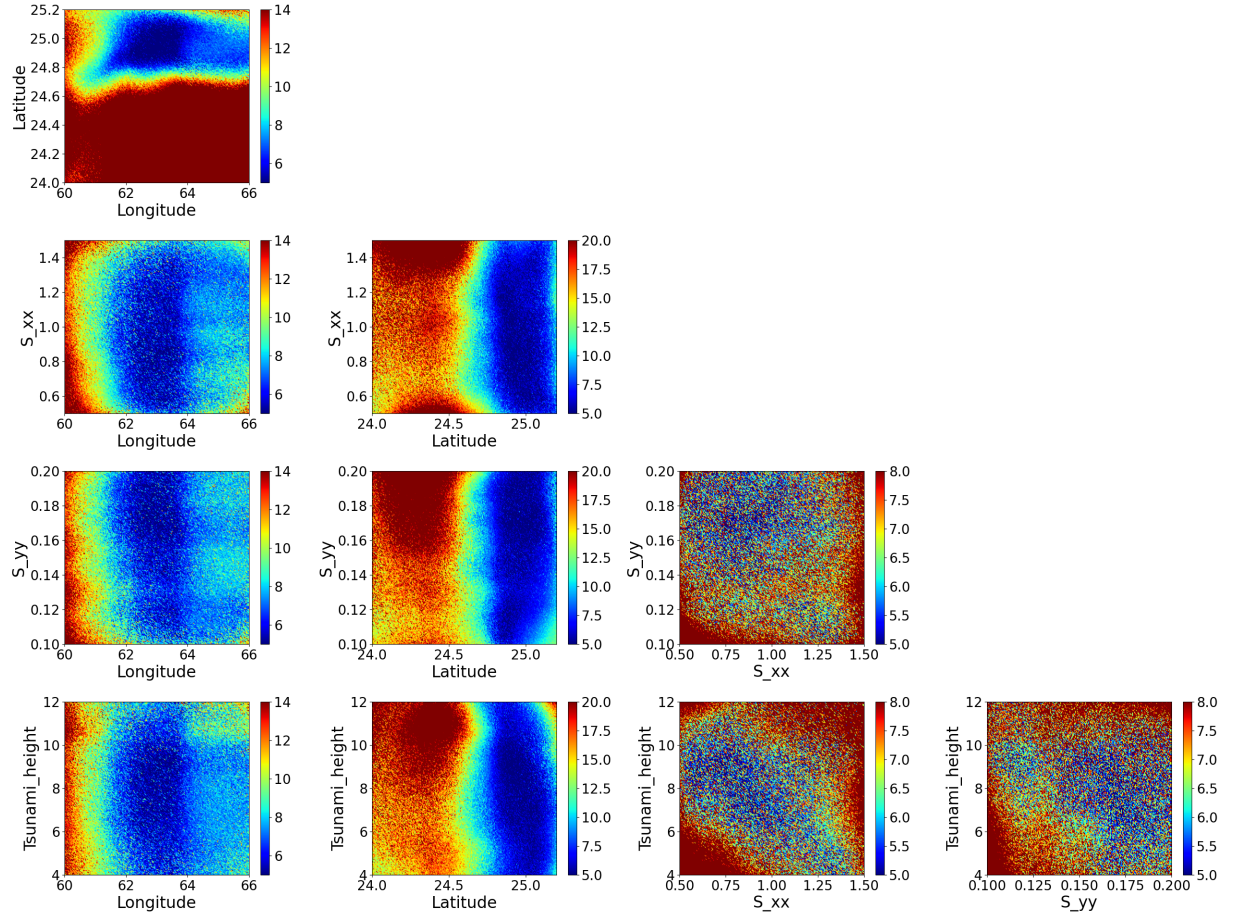


Figure 4: Two-dimensional projected distribution of Implausibility for wave 1.

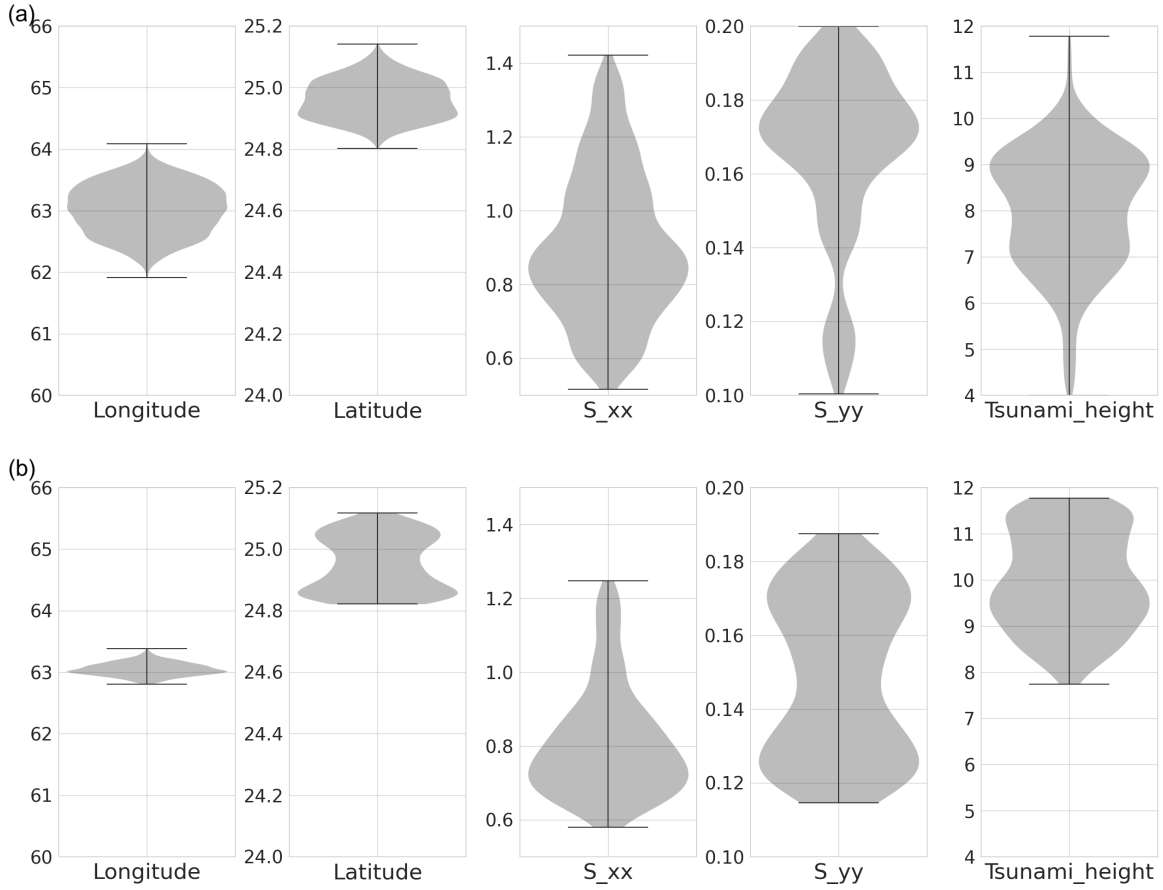


Figure 5: Violin plots of each parameter in NROY in wave1 and wave 2.

of FHM.

We re-implement FHM using parameter values from Θ_1 , built as a five-dimensional hypercube defined by the upper and lower bounds of each parameter NROY region in wave 1 (as in the violin plot of panel (a) of Fig. 5). The results for wave 2 are depicted in Panel (b) in Figure 5. A significant restriction has been obtained on the tsunami height in wave 2 compared to wave 1. The areas excluded in S_{xx} and S_{yy} , which were almost not yet eliminated in wave 1, have substantially increased in wave 2. Additionally, the NROY region for the longitude parameter has been greatly narrowed down to nearly a precise value.

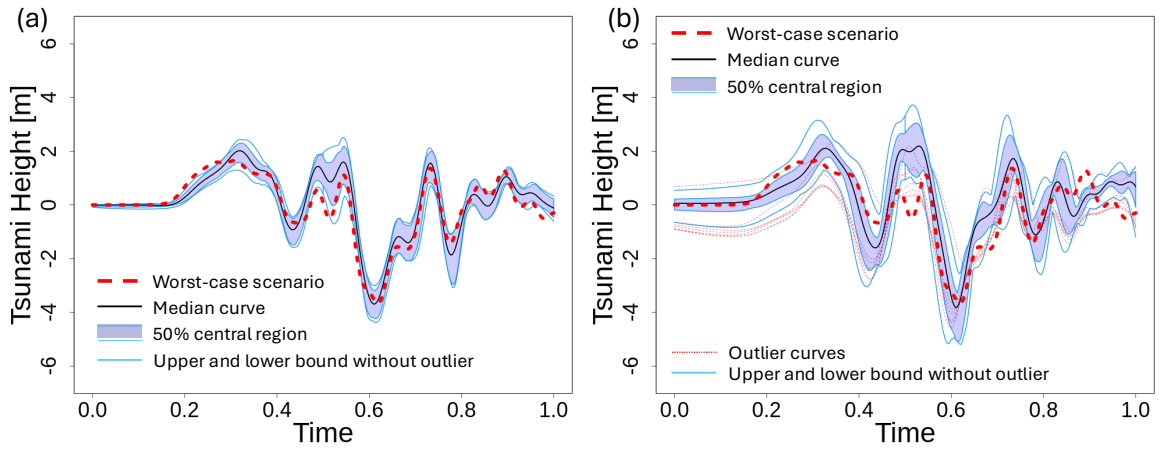


Figure 6: Tsunami forecasting at Mumbai 001 observation point with functional history matching (Panel (a)) and landmark-based history matching (Panel (b)). The horizontal axis represents time, converting the 90-minute interval from 14:30 to 16:00 into $[0, 1]$ range.

3.5 Forecasting and Comparison.

The foremost importance of this method lies in its ability to forecast tsunami time series data. When using the Wave 2 result to forecast tsunami time series data at the Mumbai 001 observation point, only 497 emulated curves are selected as non-implausible. Panel (a) of Figure 6 displays the functional boxplot (Sun & Genton 2011) of these forecasted curves. It is apparent that both the 50% central region, indicated by the blue area, and the median curve, represented by the thin black line, demonstrate shapes that are remarkably similar to the worst-case scenario. Furthermore, the upper and lower bounds of the selected emulation curves, represented by the thin blue lines, are confined to a very narrow range, confirming the absence of outlier curves.

We compare our functional history matching method with the traditional method, landmark-based history matching. In the landmark-based approach, selecting specific features from the tsunami time series data is critical. For this analysis, to independently apply the common history matching method, we identify the four most representative features in the tsunami time series data: the

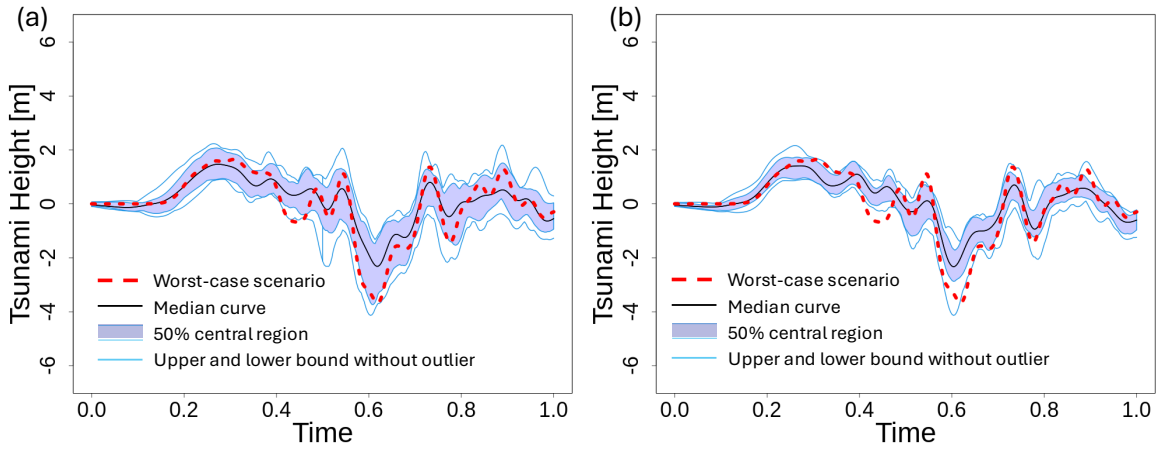


Figure 7: Tsunami forecasting at Mumbai 001 point with functional history matching in wave 1. Panel (a) is based on data from four DART observation points, while Panel (b) includes these DART points plus the virtual observation point. The horizontal axis is the same as in Figure 6.

maximum value (in meters), minimum value (in meters), the time elapsed to reach the maximum value (in seconds), and the time elapsed to reach the minimum value (in seconds). As illustrated in Panel (b) of Figure 6, landmark-based history matching selects 306 emulated curves; however, this approach is less effective compared to functional history matching. Specifically, the range bounded by the upper and lower limits of the emulation curves has significantly expanded. The area of this region, referred to as the amplitude, is 0.99 in functional history matching, whereas it more than doubles to 2.48 in landmark-based history matching. Landmark-based history matching also fails to adequately capture the decrease in tsunami height around 0.5, 0.7, and 1.0 on the horizontal axis, as well as the increase near 0.9. Additionally, it was confirmed that landmark-based history matching results in the selection of outlier curves.

An analysis was performed to examine the impact of adding virtual observation points, depicted in Figure 2, on tsunami forecasting. The virtual observation point is positioned on the opposite side of the DART observation points and is thought to contribute to the reduction of the NROY parameter subspace. When comparing the results from Wave 1 at Mumbai 001 observation point,

as illustrated in Panel (a) of Figure 7, using only four DART observation points allows for a rough forecasting of the tsunami shape, yet the range is wider. This is likely because the selected 2,381 emulation curves include some that deviate slightly from the worst-case scenario. On the other hand, the addition of the virtual observation point resulted in the selection of 342 emulation curves for Wave 1, leading to a narrower forecasted tsunami width as shown in Panel (b). These results suggest that virtual observation points significantly contribute to the selection of non-implausible input parameter values. For further details at observation points 002, 003, and 004, see the supplemental material. The time required for several key computations in this method is shown in Table 1. The JAGURS simulates a single tsunami, performed over an area with longitudes [62, 74] and latitudes [14, 26], at a spatial resolution of 15 arc seconds and a temporal resolution of 1.5 s, over a six-hour period, takes around 841 s. OPE training is conducted using five parameters, employing results from 100 simulations. Emulation involves estimating a mean curve for a new set of parameter values, and also includes sampling a curve and computing its derivative. Random Projection generates a random function, takes the inner product of this function with both an emulated curve and the worst-case tsunami, and computes the distance between the emulated curve and the worst-case scenario. These calculations were repeated 20 times, and the mean and standard deviation were computed. The aforementioned computational

Table 1: Computational Time.

	Tsunami Simulation	Emulator Training	Emulation	Random Projection
Average [s]	841.631	0.046	0.098	0.015
Standard Deviation [s]	4.462	0.009	0.008	0.002

procedures must be repeated as many times as necessary for functional history matching, and all these processes can be parallelized. Given the 120-minute margin between the latest observation

time at the DART stations used for emulator training and the earliest forecast time for Mumbai, it is feasible to issue tsunami warnings well in advance during actual operations.

4 Discussion and Conclusion

History matching techniques have been used for various types of data, and a remarkable technique has been developed recently by rotating the basis vectors of SVD and combining NROY estimation with probabilistic calibration after high-dimensional discrete outputs are projected onto low-dimensional space (Salter et al. 2019). However, these developments are designed for discrete output, not for functional data such as curves and surfaces, which are natural outputs of physical systems. In this paper, we developed a functional history matching method targeting infinite-dimensional data. We successfully applied this new approach to a tsunami forecasting case study, using JAGURS tsunami simulation at DART observation points, under conditions where accurate initial tsunami information was unavailable. The reason for using tsunami data at DART observation points is to demonstrate that the rapid and accurate tsunami time-series forecasting method we propose can be directly applied to actual observational data. This is feasible because the National Data Buoy Center (NDBC) receives DART data in real-time, and it is archived by the National Centers for Environmental Information (NCEI), making the proposed framework applicable.

Conventional landmark-based history matching allows for broad tsunami forecasting, yet it fails to accurately capture several local peaks and troughs. Our method, which can effectively utilize the entire tsunami waveform, shows excellent skills in this regard. The result demonstrates that our method effectively captures sea surface velocity changes (phase information) by treating observational data as infinite-dimensional functional data, significantly reduces computational load through the use of a functional emulator, considers model discrepancies between the simple ini-

tial tsunami model and the actual tsunami shape, and has a capability to compute forecast values with uncertainty. Our method does not rely on seismic information nor require an extensively vast pre-existing tsunami database, making it an effective approach even for tsunamis triggered by submarine landslides and for regions without prior tsunami databases.

To facilitate further research using this new method, we present a case study involving an additional observation point on the opposite side of the DART observation locations. It has been confirmed that placing this hypothetical observation point improves the quality of forecasting in Mumbai, by facilitating the reduction of the NROY subspace. These findings suggest that, when combined with optimization techniques, our method is capable of providing solutions for the optimal placement of observation points necessary for high-accuracy tsunami forecasting worldwide, using only computational experiments.

In summary, we introduced a new approach called functional history matching, demonstrated its effectiveness in forecasting tsunamis, and confirmed its real-time analysis capability with a reasonable computation cost. Combining our method with other predictive approaches can lead to more accurate tsunami warnings, potentially saving many lives.

Supplemental material The supplementary figures, tables, and explanations referenced in the main text are included in a PDF file.

Program codes The necessary codes are available on the first author's website.

Disclosure Statement The authors report there are no competing interests to declare.

Funding XXXXX.

Acknowledgments XXXXX.

References

- Andrianakis, I., Vernon, I. R., McCreesh, N., McKinley, T. J., Oakley, J. E., Nsubuga, R. N., Goldstein, M. & White, R. G. (2015), ‘Bayesian history matching of complex infectious disease models using emulation: a tutorial and a case study on hiv in uganda’, *PLoS computational biology* **11**(1), e1003968.
- Baba, T., Allgeyer, S., Hossen, J., Cummins, P. R., Tsushima, H., Imai, K., Yamashita, K. & Kato, T. (2017), ‘Accurate numerical simulation of the far-field tsunami caused by the 2011 tohoku earthquake, including the effects of boussinesq dispersion, seawater density stratification, elastic loading, and gravitational potential change’, *Ocean Modelling* **111**, 46–54.
- Baba, T., Takahashi, N., Kaneda, Y., Ando, K., Matsuoka, D. & Kato, T. (2015), ‘Parallel implementation of dispersive tsunami wave modeling with a nesting algorithm for the 2011 tohoku tsunami’, *Pure and Applied Geophysics* **172**, 3455–3472.
- Biau, G., Devroye, L. & Lugosi, G. (2008), ‘On the performance of clustering in hilbert spaces’, *IEEE Transactions on Information Theory* **54**(2), 781–790.
- Craig, P., Goldstein, M., Seheult, A. H. & Smith, J. A. (1996), ‘Bayes linear strategies for matching hydrocarbon reservoir history’, *Bayesian statistics* **5**, 69–95.
- Cuesta-Albertos, J. A., del Barrio, E., Fraiman, R. & Matrán, C. (2007), ‘The random projection method in goodness of fit for functional data’, *Computational Statistics & Data Analysis* **51**(10), 4814–4831.
- Cuesta-Albertos, J. A., Fraiman, R. & Ransford, T. (2006), ‘Random projections and goodness-of-fit tests in infinite-dimensional spaces’, *Bulletin of the Brazilian Mathematical Society* **37**(4), 477–501.

- Cuesta-Albertos, J. A., Fraiman, R. & Ransford, T. (2007), ‘A sharp form of the cramér–wold theorem’, *Journal of Theoretical Probability* **20**(2), 201–209.
- Cuesta-Albertos, J. A. & Nieto-Reyes, A. (2008), ‘The random tukey depth’, *Computational Statistics & Data Analysis* **52**(11), 4979–4988.
- Dasgupta, S. (2013), ‘Experiments with random projection’, *arXiv preprint arXiv:1301.3849* .
- Ehara, A., Salmanidou, D. M., Heidarzadeh, M. & Guillas, S. (2023), ‘Multi-level emulation of tsunami simulations over cilacap, south java, indonesia’, *Computational Geosciences* **27**(1), 127–142.
- Ferreira, C. J., Vernon, I., Caiado, C., Formentin, H. N., Avansi, G. D., Goldstein, M. & Schiozer, D. J. (2020), ‘Efficient selection of reservoir model outputs within an emulation-based bayesian history-matching uncertainty analysis’, *SPE journal* **25**(04), 2119–2142.
- Gica, E., Spillane, M. C., Titov, V. V., Chamberlin, C. D. & Newman, J. C. (2008), ‘Development of the forecast propagation database for NOAA’s short-term inundation forecast for tsunamis (SIFT)’, *NOAA technical memorandum OAR PMEL* **139**.
- Goldstein, M. & Rougier, J. (2009), ‘Reified bayesian modelling and inference for physical systems’, *Journal of statistical planning and inference* **139**(3), 1221–1239.
- Gonzalez, F. I., Milburn, H. M., Bernard, E. N. & Newman, J. C. (1998), Deep-ocean assessment and reporting of tsunamis (dart): Brief overview and status report, *in* ‘proceedings of the international workshop on tsunami disaster mitigation’, Vol. 19, NOAA Tokyo, Japan, p. 2.
- Gopinathan, D., Heidarzadeh, M. & Guillas, S. (2021), ‘Probabilistic quantification of tsunami current hazard using statistical emulation’, *Proceedings of the Royal Society A* **477**(2250), 20210180.

- Gopinathan, D., Venugopal, M., Roy, D., Rajendran, K., Guillas, S. & Dias, F. (2017), ‘Uncertainties in the 2004 sumatra–andaman source through nonlinear stochastic inversion of tsunami waves’, *Proceedings of the Royal Society A: Mathematical, Physical and Engineering Sciences* **473**(2205), 20170353.
- Guillas, S., Sarri, A., Day, S. J., Liu, X. & Dias, F. (2018), ‘Functional emulation of high resolution tsunami modelling over Cascadia’, *The Annals of Applied Statistics* **12**(4), 2023 – 2053.
- Johnson, J. S., Regayre, L. A., Yoshioka, M., Pringle, K. J., Turnock, S. T., Sexton, D. M., Rostron, J. W., Schutgens, N. A., Partridge, D. G., Liu, D. et al. (2020), ‘Robust observational constraint of uncertain aerosol processes and emissions in a climate model and the effect on aerosol radiative forcing’, *Atmospheric Chemistry and Physics* **20**(15), 9491–9524.
- Kennedy, M. C. & O’Hagan, A. (2001), ‘Bayesian calibration of computer models’, *Journal of the Royal Statistical Society: Series B (Statistical Methodology)* **63**(3), 425–464.
- Kruger, W. (1961), ‘Determining areal permeability distribution by calculations’, *Journal of Petroleum Technology* **13**(07), 691–696.
- Lay, T., Kanamori, H., Ammon, C. J., Nettles, M., Ward, S. N., Aster, R. C., Beck, S. L., Bilek, S. L., Brudzinski, M. R., Butler, R. et al. (2005), ‘The great sumatra-andaman earthquake of 26 december 2004’, *science* **308**(5725), 1127–1133.
- Loeppky, J. L., Sacks, J. & Welch, W. J. (2009), ‘Choosing the sample size of a computer experiment: A practical guide’, *Technometrics* **51**(4), 366–376.
- Loh, W.-L. (1996), ‘On latin hypercube sampling’, *The annals of statistics* **24**(5), 2058–2080.
- Marron, J. S., Ramsay, J. O., Sangalli, L. M. & Srivastava, A. (2015), ‘Functional data analysis of amplitude and phase variation’, *Statistical Science* pp. 468–484.

- McKay, M. D., Beckman, R. J. & Conover, W. J. (1979), 'A comparison of three methods for selecting values of input variables in the analysis of output from a computer code', *Technometrics* **21**(2), 239–245.
- Nieto-Reyes, A. & Battey, H. (2016), 'A topologically valid definition of depth for functional data'.
- Okal, E. A. (1988), 'Seismic parameters controlling far-field tsunami amplitudes: A review', *Natural Hazards* **1**(1), 67–96.
- O'Hagan, A. (2006), 'Bayesian analysis of computer code outputs: A tutorial', *Reliability Engineering & System Safety* **91**(10-11), 1290–1300.
- Percival, D. M., Percival, D. B., Denbo, D. W., Gica, E., Huang, P. Y., Mofjeld, H. O. & Spillane, M. C. (2014), 'Automated tsunami source modeling using the sweeping window positive elastic net', *Journal of the American Statistical Association* **109**(506), 491–499.
- Polet, J. & Kanamori, H. (2000), 'Shallow subduction zone earthquakes and their tsunamigenic potential', *Geophysical Journal International* **142**(3), 684–702.
URL: <https://doi.org/10.1046/j.1365-246x.2000.00205.x>
- Pukelsheim, F. (1994), 'The three sigma rule', *The American Statistician* **48**(2), 88–91.
- Ramsay, J. O. (1982), 'When the data are functions', *Psychometrika* **47**, 379–396.
- Ramsay, J. O. & Silverman, B. W. (2005a), *Fitting differential equations to functional data: Principal differential analysis*, Springer.
- Ramsay, J. O. & Silverman, B. W. (2005b), *Functional Data Analysis*, Springer.
- Rougier, J. (2008), 'Efficient emulators for multivariate deterministic functions', *Journal of Computational and Graphical Statistics* **17**(4), 827–843.

- Rougier, J., Guillas, S., Maute, A. & Richmond, A. D. (2009), ‘Expert knowledge and multi-variate emulation: The thermosphere–ionosphere electrodynamics general circulation model (tie-gcm)’, *Technometrics* **51**(4), 414–424.
- Salter, J. M., Williamson, D. B., Scinocca, J. & Kharin, V. (2019), ‘Uncertainty quantification for computer models with spatial output using calibration-optimal bases’, *Journal of the American Statistical Association* .
- Sarri, A., Guillas, S. & Dias, F. (2012), ‘Statistical emulation of a tsunami model for sensitivity analysis and uncertainty quantification’, *Natural Hazards and Earth System Sciences* **12**(6), 2003–2018.
- Sun, Y. & Genton, M. G. (2011), ‘Functional Boxplots’, *Journal of Computational and Graphical Statistics* **20**(2), 316–334.
URL: <https://doi.org/10.1198/jcgs.2011.09224>
- Tang, L., Titov, V. V., Moore, C. & Wei, Y. (2017), ‘Real-time assessment of the 16 september 2015 chile tsunami and implications for near-field forecast’, *The Chile-2015 (Illapel) Earthquake and Tsunami* pp. 267–285.
- Vempala, S. S. (2005), *The random projection method*, Vol. 65, American Mathematical Soc.
- Vernon, I., Goldstein, M. & Bower, R. (2014), ‘Galaxy formation: Bayesian history matching for the observable universe’, *Statistical science* pp. 81–90.
- Wang, J.-L., Chiou, J.-M. & Müller, H.-G. (2016), ‘Functional data analysis’, *Annual Review of Statistics and its application* **3**, 257–295.
- Wang, Y., Tsushima, H., Satake, K. & Navarrete, P. (2021), ‘Review on recent progress in near-

field tsunami forecasting using offshore tsunami measurements: Source inversion and data assimilation’, *Pure and Applied Geophysics* **178**, 5109–5128.

William, B. J. & Lindenstrauss, J. (1984), ‘Extensions of lipschitz mapping into hilbert space’, *Contemporary mathematics* **26**(189-206), 323.

Williamson, D. B., Blaker, A. T. & Sinha, B. (2017), ‘Tuning without over-tuning: parametric uncertainty quantification for the nemo ocean model’, *Geoscientific Model Development* **10**(4), 1789–1816.

Williamson, D., Blaker, A. T., Hampton, C. & Salter, J. (2015), ‘Identifying and removing structural biases in climate models with history matching’, *Climate dynamics* **45**, 1299–1324.

Xu, W., Williamson, D. B., Hourdin, F. & Roehrig, R. (2023), ‘Feature calibration for computer models’, *arXiv preprint arXiv:2310.18875* .

Functional history matching for tsunami warnings: supplemental material

1. WORST-CASE SCENARIO TSUNAMI TIME SERIES DATA AND DATA PRE-PROCESSING

This study analyzes the worst-case scenario tsunami that could occur off the Makran coast, as studied in [Gopinathan et al. \(2021\)](#) and described in Fig. S1 and S2. Fig. S2 shows the same tsunami from different angles. As shown in these figures, the rise and fall of the sea level occur simultaneously but have different shapes; they are not mirror images of each other. In addition, each phase, whether rising or falling, has an asymmetric waveform when considered on its own. This waveform asymmetry persists under any time shift or rescaling and cannot be accurately reproduced using a Gaussian shaped waveform. We performed tsunami simulations in this area using the JAGURS simulator ([Baba et al. 2015, 2017](#)). The resolution of both the bathymetry and tsunami input files for the simulation is set to 15 arcseconds. The time step for the tsunami simulation depends on the bathymetry resolution and the maximum seabed depth, as expressed in Equation S1.

$$dt \simeq \frac{\Delta x}{\sqrt{2gh}}, \quad (\text{S1})$$

where dt is the time resolution (seconds), Δx is the resolution of the bathymetry file (meters), g is the gravitational acceleration (9.8m/s^2), and h is the maximum depth (meters). For this target area, we confirmed that JAGURS could perform calculations without any problems with $dt = 1.5$. Therefore, all calculations were executed with $dt = 1.5$.

To apply functional history matching in this study, it is necessary to restrict the time window of the tsunami observations. Analyzing intervals with no sea-level change is not informative, and using the entire observation period would incur unnecessary computational cost. Hence, it is more efficient to analyze a limited range. Therefore, a limited time window was used. As described in the main text, a 30-minute interval was extracted at four DART stations (buoys): DART23228 from 10:30 to 11:00, DART23226 from 10:50 to 11:20, DART23225 from 11:05 to 11:35, and DART23011 from 11:30 to 12:00. In the tsunami simulations, the simulation time step dt in JAGURS was set to 1.5 s, which yields 1201 samples per 30-minute interval when both endpoints are included. We then downsampled each observed time series by a factor of 12, sampling every twelfth point, to preserve the overall waveform shape, resulting in 101 samples per interval for analysis. For the virtual observation point indicated by a black circle in Figure S1, a 30 minute

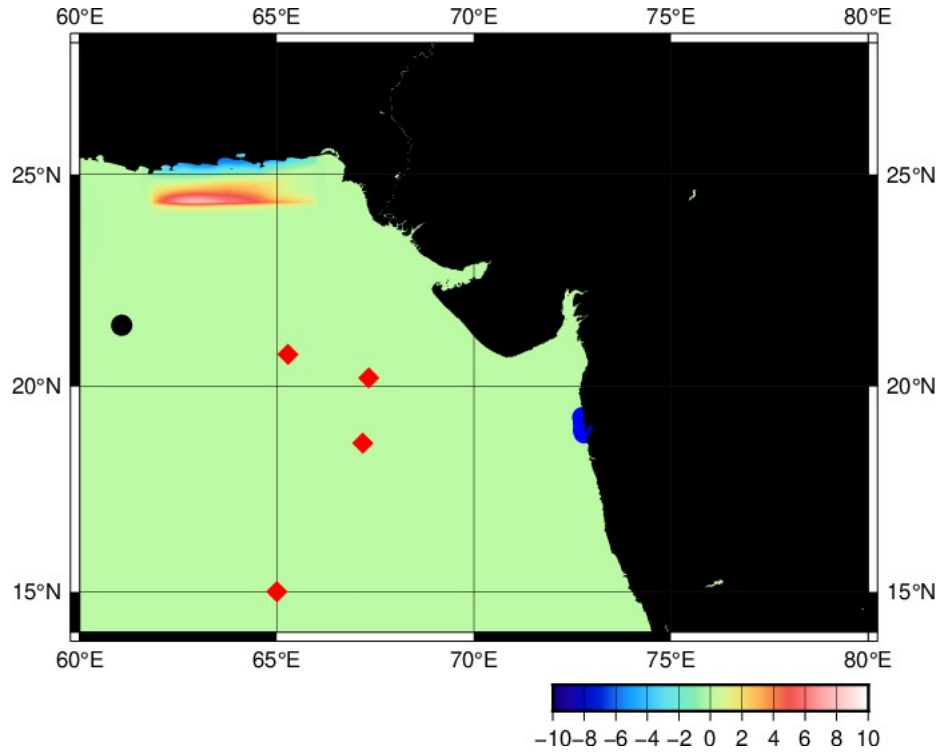


Fig. S1. A two-dimensional diagram of a tsunami in a worst-case scenario. Black represents the land, light green represents the sea surface, red indicates sea level rise due to the tsunami, and blue indicates sea level fall caused by the tsunami.

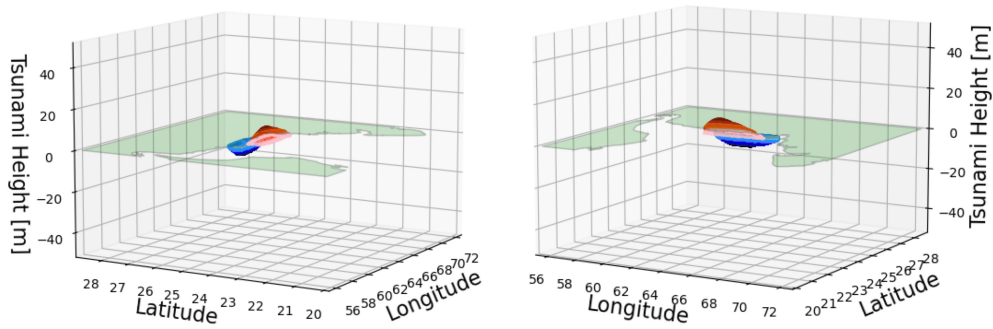


Fig. S2. The worst-case scenario tsunami from different angles. The green color represents land, the red color indicates sea level rise, and the blue color represents sea level fall.

interval from 10:30 to 11:00 was extracted and downsampled in the same way, yielding 101 samples for analysis.

For forecasting in Mumbai, we extracted a 90-minute interval from 14:30 to 16:00 at observation points 001 and 002, yielding 3,601 samples per point when both endpoints are included, and a 120-minute interval from 14:00 to 16:00 at observation points 003 and 004, yielding 4,801

samples per point. We then downsampled each time series by a factor of 12, retaining every twelfth point to preserve the overall waveform shape, resulting in 301 samples per point for observation points 001 and 002 and 401 samples per point for observation points 003 and 004. The selected analysis windows for these observation points, the virtual observation point, and the forecast points in Mumbai are shown in Figure 1 in the main paper as shaded and hatched regions. The extracted time series were then represented in functional form using a B-spline basis.

To perform functional emulation using Outer Product Emulator (OPE) (Rougier 2008), it is necessary to determine the correlation lengths λ_{j_θ} and λ_t for $\kappa_\lambda^\theta(\theta, \theta')$ and $\kappa_\lambda^t(t, t')$, respectively, as defined in Equations 9 and 10 of the main paper. The training data used to construct the emulator comprised the 30-minute intervals described above, which were rescaled to the $[0, 1]$ range. Similarly, all simulation input parameters (longitudes and latitudes of the rising and falling tsunami centers, standard deviations in the longitude and latitude directions, and the maximum tsunami height) were rescaled to the $[0, 1]$ range. On this basis, we assumed a uniform correlation length λ_θ across all parameters and estimated its value. The procedure was as follows. First, we performed five additional tsunami simulations with JAGURS that were not included in the ensemble used to train the emulator. Next, using the input parameter values from these additional simulations, we emulated the corresponding tsunami time series with an OPE trained on the aforementioned ensemble. We then compared the outputs of the JAGURS simulations with those from the OPE emulation. During this process, we considered 50 candidate values for each of λ_θ and λ_t , ranging from 0.1 to 9.9 in increments of 0.2, and selected the three value pairs that yielded the smallest root mean square error (RMSE) for each tsunami time series. This procedure was applied at each of the four DART observation points. Consequently, a total of 60 value pairs were selected from the 2,500 potential combinations. We then took the average of these selected pairs as the estimates of the correlation lengths λ_{j_θ} and λ_t . The resulting correlation lengths were as follows: for Wave 1, $\lambda_\theta = 1.143$ and $\lambda_t = 1.956$; for Wave 2, $\lambda_\theta = 0.896$ and $\lambda_t = 1.700$.

2. SENSITIVITY ANALYSIS

To assess the validity of the emulator selected by the RMSE criterion, we conducted a sensitivity analysis. We varied one input parameter at a time while holding the other four fixed and examined the resulting outputs. The sensitivity analysis results at the DART23228 observation point are shown in Figure S3. Varying an input parameter changes the shape of the tsunami time series. However, these changes do not produce qualitatively different waveforms or implausible outputs. These observations provide preliminary evidence that the emulator was constructed successfully. It is important to note, however, that apparent adequacy at this stage does not guarantee that the emulator will reproduce the simulator outputs for arbitrary input settings.

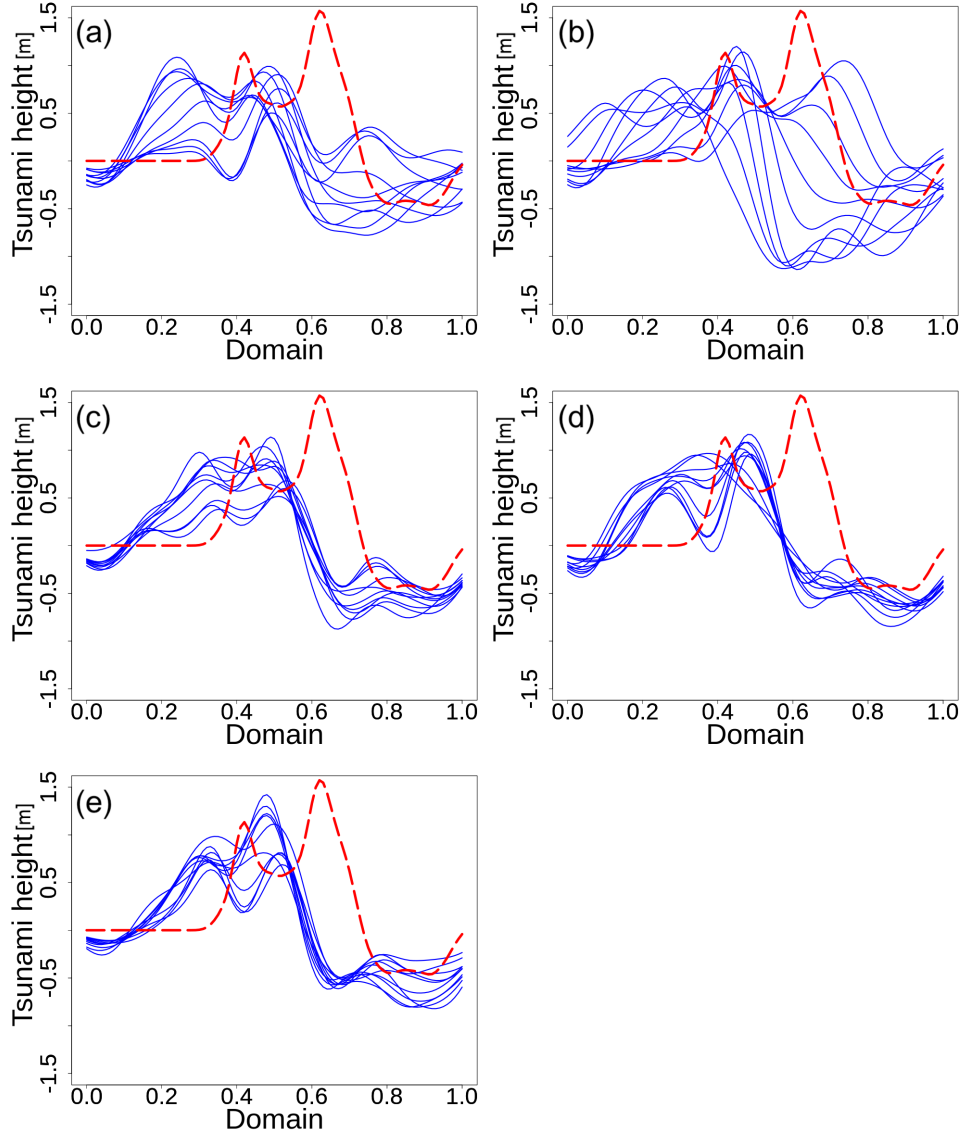


Fig. S3. Sensitivity analysis at the location of DART 23228. The worst-case scenario (thick dashed line) and variations of each parameter from their minimum to maximum values at equal intervals, are shown in 10 changes (thin solid lines). The varying parameter in each panel is (a) longitude, (b) latitude, (c) S_{xx} , (d) S_{yy} , and (e) the maximum tsunami height, respectively.

Upon further observation of how tsunami time series shapes respond to changes in parameter inputs, it is clear that the latitude parameter causes the most significant alterations in the case of the wave 1 emulator as displayed in Panel (b) in Figure S3. Based on this finding, it is conjectured that the parameter θ_2 could be reduced relatively more than other parameters in wave 1. The

longitude parameter, θ_1 , has the second greatest impact on the variability of the emulator output following the latitude parameter. Thus, in wave 1, it is expected that θ_1 also tends to have a smaller non-implausible region. These inferences can be confirmed as correct by the violin plots of the NROY subspace in Figure 6 of the main paper, which show that the NROY spaces for θ_1 and θ_2 are the most reduced. On the other hand, this sensitivity analysis for S_{xx} , S_{yy} , and the tsunami height suggests that the shape changes minimally with variations leading to the hypothesis that the parameter space may not be significantly reduced in direction θ_3 , θ_4 , and θ_5 . The validity of these conjectures is also confirmed through violin plots of wave 1.

For Wave 2, we build an emulator using a different set of simulation ensembles with input parameter values from Θ_1 . Consequently, it is presumed that the directions susceptible to reduction in this reduced subspace are different from those in wave 1. The comparison of violin plots from wave 1 and wave 2 allows for the verification of this conjecture.

3. DISTANCE EVALUATION BETWEEN FUNCTIONS

The next step in computing implausibility is to evaluate the similarity between the emulated curves and the worst-case tsunami time series. Numerous methods exist for evaluating similarity or distance between functions. Examples include methods for assessing similarity between functions in functional-data clustering (Ferreira & Hitchcock 2009) and for clustering sparsely sampled functional data (James & Sugar 2003). In addition, there are comparative studies of similarity and distance measures (Tokushige et al. 2003). Later work examined preprocessing to improve clustering (Hitchcock et al. 2006) and addressed phase variation (Marron et al. 2015).

A. L_p Norm

A basic measure of size for functions is the L^p norm, defined as follows.

$$\|f\|_p := \left(\int_S |f|^p d\mu \right)^{1/p}, \quad (\text{S2})$$

where $p = 1, 2, \dots, \infty$. The induced distance between functions is $d_p(f, g) = \|f - g\|_p$. However, in some settings, these norms are not ideal for assessing similarity between functional data. In particular, the L_1 and L_2 norms primarily reflect amplitude differences and do not explicitly account for phase variation. Consequently, they may fail to capture features revealed by derivatives of the functions. They integrate value differences over the domain and can yield unsatisfactory results in the presence of phase variability (Marron et al. 2015). The L_∞ norm, $\|f\|_\infty \equiv \inf\{C \geq 0 : |f(x)| \leq C \text{ for almost every } x\}$, emphasizes the maximum absolute deviation over the domain and does not capture phase variation. Functional data exhibit both amplitude and phase variation, such as changes in peak and trough locations, which are central

to this study. Therefore, L_p based distances are not well suited to our objectives, which require accounting for phase variation.

B. Dynamic Time Warping and Fréchet distance

Other techniques include Dynamic Time Warping (DTW) (Sakoe & Chiba 1978) and the Fréchet distance (Alt & Godau 1995), which are widely used for time-series similarity. Both operate on discretized time series: DTW minimizes an alignment cost between two sequences, whereas the Fréchet distance measures the maximum of the shortest distances along an optimal traversal of the curves Brankovic et al. (2020). However, several issues limit their use here. First, tsunami analysis requires real-time processing, yet these methods can be computationally intensive. Second, while DTW aligns sequences by allowing phase shifts, the resulting distance primarily reflects amplitude differences after alignment; quantifying phase similarity would require analyzing the warping function and propagating uncertainty, which is computationally demanding. Similarly, while the Fréchet distance permits monotone time reparameterization, it emphasizes the maximal discrepancy along an optimal traversal and is sensitive to noise and sampling density. Moreover, it does not naturally propagate emulator or observational uncertainty, and its pairwise computational cost is prohibitive in our large scale, near real time setting. Because the goal is timely warning, methods that do not efficiently incorporate peak and trough timing under uncertainty are not aligned with our objectives.

C. Sobolev Norm

The Sobolev norm provides an alternative that incorporates derivatives up to order k , not just the first derivative. The Sobolev space $W^{k,p}$ consists of functions whose derivatives up to order k lie in L^p space. For $p = 2$, $W^{k,2}$ is a Hilbert space H^k with norm

$$\|f\|_{k,2} := \left(\sum_{i=0}^k \int_{\mathbb{T}} \left| \frac{d^i f(t)}{dt^i} \right|^2 dt \right)^{1/2}. \quad (\text{S3})$$

However, the computational cost of the Sobolev norm is even higher than that of the L_2 norm, and as the degree of differentiation k increases, the Sobolev norm value also continues to increase, making it difficult to handle. In our setting, distances feed into the implausibility calculation in Equation 1 of the main paper to separate implausible from non-implausible regions. The purpose is then to use the calculated implausibility to separate the implausible and non-implausible parameter subspace based on a certain threshold. Changing k alters the norm and can shift threshold based decisions, risking misclassification of regions. Because we lack a principled and computationally feasible rule for choosing k , and decisions are sensitive to this choice, Sobolev based distances are not well suited to our screening objective.

D. Functional Principal Component Analysis

Another approach is to project functional data and compare distances between the resulting scores. We consider functional principal component analysis (FPCA) ([Ramsay & Silverman 2005](#)), a standard tool in functional data analysis. As discussed in the main paper, FPCA alone is inadequate for our objective. Let $X(t) \in L^2[0, 1]$ with mean

$$\mu(t) = E[X(t)] \quad (\text{S4})$$

and covariance

$$\Gamma(s, t) = \text{Cov}(X(s), X(t)) \quad (\text{S5})$$

Then, the covariance operator can apply to functions $f(t)$ in $L^2[0, 1]$.

$$(\Gamma f)(t) = \int_{s \in [0, 1]} f(s) \Gamma(t, s) ds \quad (\text{S6})$$

Given the continuity of $\Gamma(s, t)$, the covariance function can be expressed as follows.

$$\Gamma(s, t) = \sum_{j=1}^{\infty} \xi_j \psi_j(s) \psi_j(t), \quad (\text{S7})$$

where ξ_j and ψ_j are eigenvalues and eigenfunctions satisfying $\Gamma \psi_j = \xi_j \psi_j$. It should be noted that ξ_j are arranged in descending order. In this case, through the Karhunen-Loève expansion ([Loeve 1948](#), [Karhunen 1947](#)), the difference between X_i and the mean function can be represented as below.

$$X_i(t) - \mu(t) = \sum_{j=1}^{\infty} \zeta_{ij} \psi_j(t), \quad (\text{S8})$$

$$\zeta_{ij} = \int_{t \in [0, 1]} (X_i(t) - \mu(t)) \psi_j(t) dt \quad (\text{S9})$$

Also, the mean and the variance of ζ_{ij} are represented as $E[\zeta_{ij}] = 0$ and $\text{Var}[\zeta_{ij}] = \xi_j$, respectively ([Hall et al. 2006](#)). This expansion is also referred to as the functional principal component expansion.

For comparison, we applied the following FPCA based procedure. First, following our functional history matching procedure, we sampled 100 parameter settings using Latin hypercube sampling and ran the corresponding JAGURS simulations with those settings. Next, we trained an OPE based emulator on this ensemble, then generated 1,000,000 distinct input settings by Latin hypercube sampling and evaluated the emulator at each DART point, yielding one million emulated time series per point. We then applied FPCA to the emulated curves and the worst-case scenario curve, obtaining principal component scores for each principal direction and the contribution of each principal component. At DART23228, the first two principal components

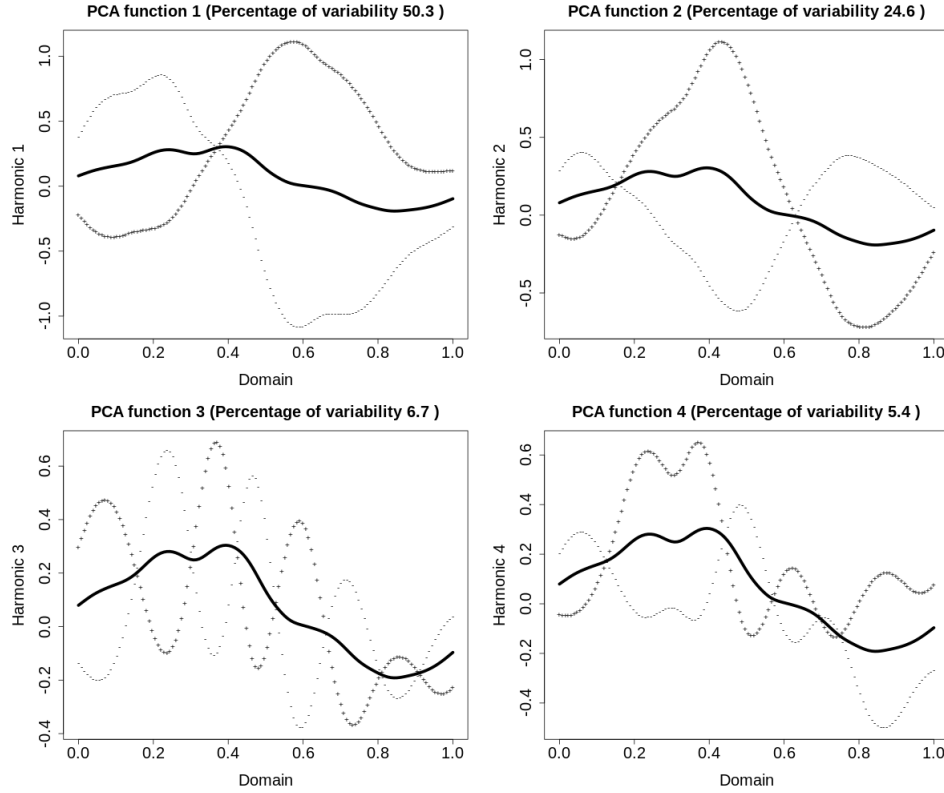


Fig. S4. Results of FPCA applied to tsunami emulation data and worst-case scenario time series data at the DART23228 site. The bold line represents the mean function. To illustrate the variation of each principal component curve around the mean function, plus and minus signs indicate two standard deviations. The proportion of variability explained by each principal component function is presented in percentage terms.

explain about 75 percent of the total variance as illustrated in Figure S4. However, even using the first principal component scores derived from the tsunami time series data at the DART23228 observation point to calculate implausibility, it is impossible to identify implausible regions. The reason for this is clearly visualized in Figure S5. At DART23228, the first principal component scores for the emulations and the worst case lay between -0.989 and 0.804 (Figure S5). We do not interpret this range, on its own, as evidence against implausibility. Because the numerator is evaluated in FPCA score coordinates, the denominator must likewise be expressed in the same coordinates before drawing any conclusion. Given such small score differences, we cannot judge whether the implausibility is below the Chebyshev based screening threshold unless the denominator is expressed in the same FPCA score coordinates as the numerator. This means representing emulator uncertainty, observational uncertainty, and model discrepancy in that coordinate system. However, FPCA does not directly propagate the OPE induced predictive

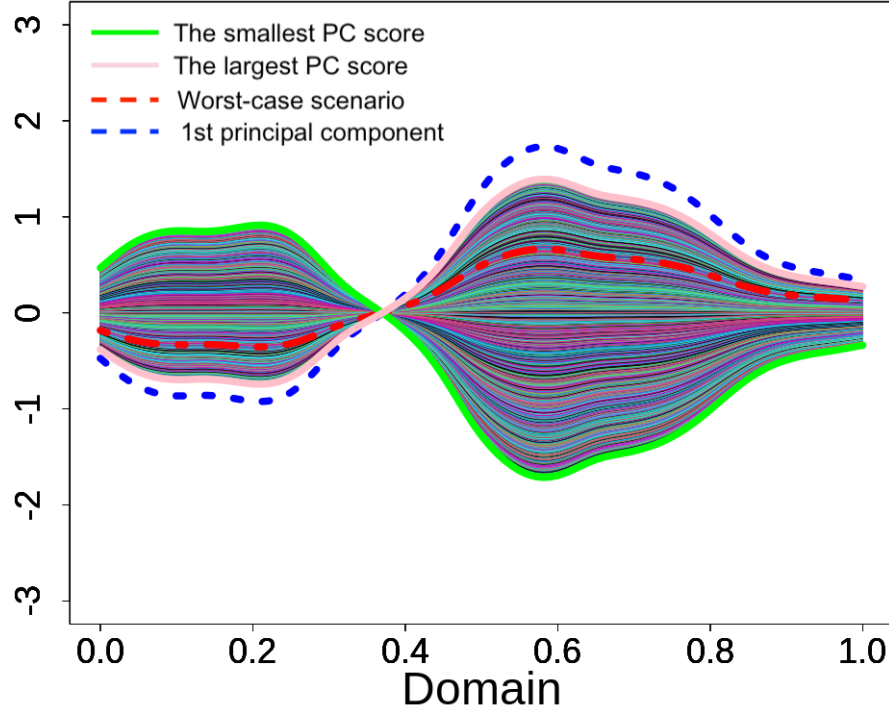


Fig. S5. Results of FPCA of one million emulation data at observation point DART23228 during Wave 1, shown against the worst-case scenario (indicated by a red dashed line). The product of the principal component scores and the first eigenfunction represents the first principal component direction of each tsunami time series data. The tsunami time series data with the highest and lowest principal component scores are indicated with thick pink and green lines, respectively. The principal component function is shown as a blue dashed line.

uncertainties into the score coordinates. In practice, this would require computing, for each emulated curve, the uncertainty along the first principal component (and similarly for additional components), which is computationally prohibitive at the scale required for near real time analysis. Consequently, we do not adopt FPCA based implausibility.

E. Reproducing Kernel Hilbert Space projection

Another strategy is to project infinite dimensional functions into a finite dimensional Reproducing Kernel Hilbert Space (RKHS) (Berlinet & Thomas-Agnan 2011). With a reproducing kernel Hilbert space \mathcal{H}_k and an orthonormal basis $\{\phi_i\} \in \mathcal{H}_k$, each function is represented by the truncated expansion

$$f(t) = \sum_{i=1}^d \lambda_i \phi_i, \quad \lambda_i = \langle f, \phi_i \rangle_{\mathcal{H}_k}, \quad (\text{S10})$$

where d is the projection dimension. While effective for dimensionality reduction, RKHS projections do not explicitly encode phase information. As with L_2 norms, they primarily reflect amplitude differences, so curves that are out of phase may still be judged close, whereas curves that are in phase but differ in amplitude may be judged far. To address this issue, projecting the differentiated curves of tsunami time series data into the RKHS can be an effective method. This approach allows us to obtain a set of d -dimensional discrete data, $\{\lambda'_1, \lambda'_2, \dots, \lambda'_d\}$. However, there are several challenges associated with this technique that need to be addressed in our research. Practical challenges include choosing the projection dimension d , selecting an appropriate kernel and bandwidth, and managing the computational burden for large scale comparisons. Moreover, in computing implausibility, if the numerator is computed as a distance in the RKHS coefficient space, the denominator must likewise be expressed in the same coordinates. This includes emulator uncertainty, observational uncertainty, and model discrepancy, and doing so reliably at scale is nontrivial and adds further computational cost.

F. Random Projection

To address these issues, we evaluate distances via random projection. Random projection preserves pairwise distances in expectation and concentrates with multiple projections, providing a computationally light surrogate for high-dimensional comparisons. This method has been employed in classification (Arriaga et al. 2015, Xie et al. 2016), clustering (Tasoulis et al. 2014, Zhao et al. 2016), and regression analysis (Maillard & Munos 2012, Geppert et al. 2017), demonstrating broad applicability. In our setting, a one dimensional projection is obtained by the inner product $\langle f(t), h(t) \rangle = \int f(t)h(t)dt$ with a random function h drawn from a stochastic process such as the Wiener process (Brown 1828), the Ornstein-Uhlenbeck processes (Uhlenbeck & Ornstein 1930), or fractional Brownian motion (Mandelbrot & Van Ness 1968). We use draws from the Wiener process, with the time unit set to the simulation time step, because they are simple to simulate and computationally efficient. To encode phase related information, we also apply random projection to differentiated time series. Since a single projection depends on the draw h , we compute projections for many independent random functions and use their average as a stable estimate. As shown in Figure S6, averaging 1,000 projections across diverse directions yields stable distance estimates.

4. UNCERTAINTY EVALUATION

To perform functional history matching, it is essential to calculate implausibility as seen in Equation 1 in the main paper, which requires the assessment of uncertainty. Generally, this uncertainty can be divided into three sources: those originating from emulators, those due to observational

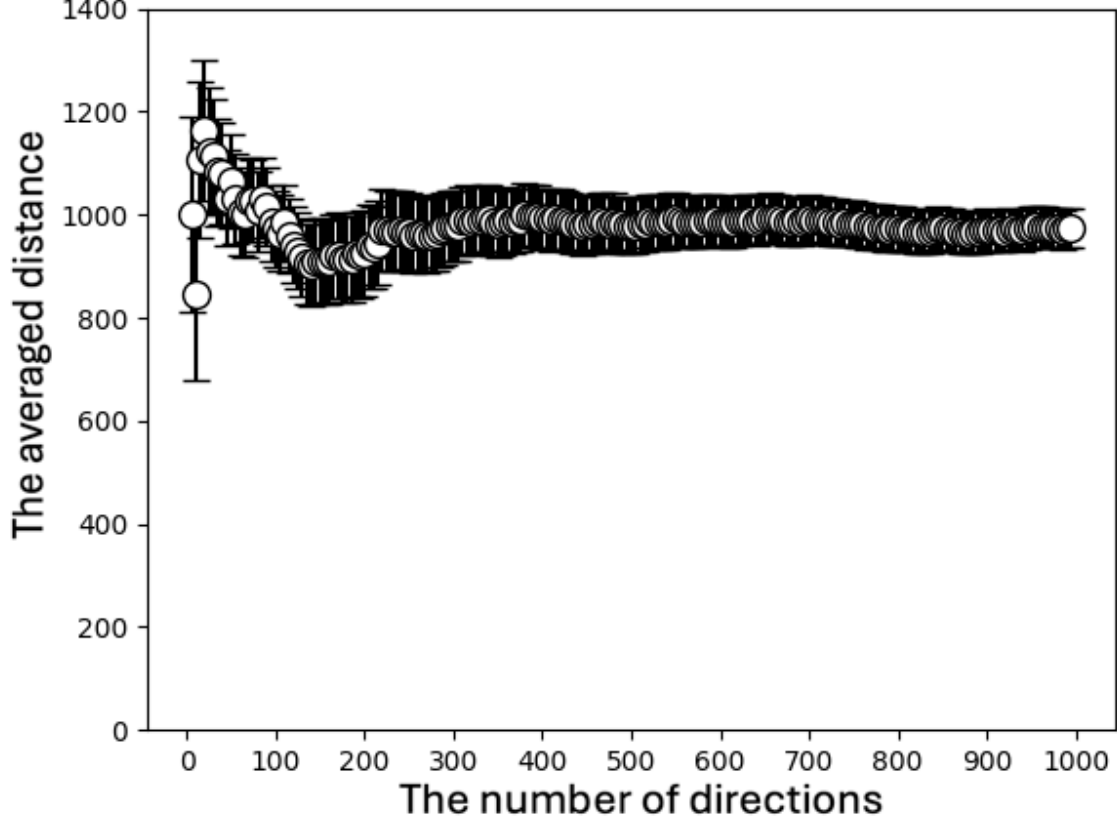


Fig. S6. The average distance between an emulation curve and the worst-case scenario curve converges using random projections. The error bars indicate $\pm\sigma$.

errors, and those due to model discrepancies. In this study, we construct an emulator using OPE and generate emulated tsunami time series data. Additionally, by differentiating these emulated time series data, we can also emulate the velocity of sea surface fluctuations. Given that OPE uses the NIG framework, the uncertainty in the emulated tsunami time series data can be determined. In this framework, the regression coefficients $\beta = (\beta_1, \beta_2, \dots, \beta_\nu)$ is modeled as a multivariate normal distribution with a covariance matrix of τV , and the error term ε is assumed to follow a Gaussian process. Consequently, given that β and ε are independent when conditioned on τ , the uncertainty in predictions $y = G\beta + \varepsilon$ is the sum of these two uncertainties,

$$V[y|\tau] = V[G\beta|\tau] + V[\varepsilon|\tau] = \tau(GVG^T + W), \quad (\text{S11})$$

where $\tau W = V[\varepsilon]$. The hyperparameter τ is modeled as an inverse gamma distribution with hyperparameters (a, d) ,

$$\text{IG}(\tau; a, d) = \frac{(d/2)^{a/2}}{\Gamma(a/2)} \tau^{-(1+a/2)} \exp \left\{ -(d/2)\tau^{-1} \right\}. \quad (\text{S12})$$

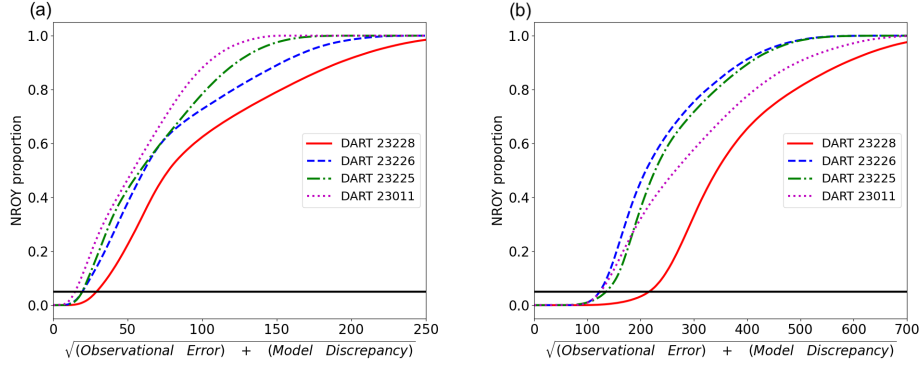


Fig. S7. Convergence of the NROY proportion for tsunami time series emulation results and their first derivatives. The horizontal axis shows the square root of observational errors plus model discrepancies. Emulator uncertainty varies across emulations; it is accounted for in the denominator but omitted from the horizontal axis for interpretability. The vertical axis is the NROY proportion.

Here, unlike the conventional notation of the inverse gamma distribution, we use an expression where $\frac{a}{2}$ and $\frac{d}{2}$ are inserted into the gamma function and exponential function, respectively, to simplify the notation following the integration of τ . Therefore, since y follows a multivariate normal distribution and its variance is known, by integrating out τ , we find that the distribution of y follows a Student's t-distribution. This procedure remains valid even when updating the distribution shapes of various parameters using observations, asserting that y still follows a Student's t-distribution. Based on these results, the variance of this t-distribution is used to represent the emulator-derived uncertainty in the calculation of implausibility. Also, in functional history matching for differentiated tsunami time series data, we evaluate the uncertainty of the emulator-derived differentiated curves at a given parameter value by sampling the tsunami time series data 1,000 times with the same parameters, differentiating each sample, and observing the variability across these 1,000 iterations. To quantify the Monte Carlo error of this estimate, we use a delta method approximation: the standard error of the standard deviation based on n emulator draws is $SE(\hat{\sigma}) \approx \hat{\sigma} / \sqrt{2(n-1)}$, so the relative standard error is $RSE(\hat{\sigma}) \approx 1 / \sqrt{2(n-1)}$ (about 2.2 % for $n = 1000$).

As described in the main paper we have calculated uncertainty based on observational error and model discrepancies using a method that divides the ensemble into k folds, following the concept of cross-validation. Specifically, this procedure seeks to establish uncertainty under conservative conditions where 5% of the elements in each fold are considered non-implausible. Using this method, it is possible to compute implausibility, thereby distinguishing between

implausible subspace and non-implausible subspace (NROY subspace). One of the methods to validate this new approach is to increase uncertainty and verify whether the proportion of NROY converges to one, as suggested in [McNeall et al. \(2016\)](#). This approach effectively confirms the relationship between uncertainty and NROY subspace as illustrated in Figure S7. In this figure, under the assumptions that observational errors are uniform at the same observation points and that model discrepancies are consistent across all simulations because of the use of the same model, the horizontal axis quantifies the uncertainty stemming from these assumed uniform model discrepancies and observation errors in all emulation curves. Figure S7 varies the square root of the sum of observational error and model discrepancy along the horizontal axis. Emulator uncertainty is included in the implausibility denominator for every emulated curve, but because it differs across curves it is held at its curve specific value and therefore is not shown on the axis. It is important to note that the uncertainty originating from emulation varies slightly among the emulation curves; therefore, a single value cannot be assigned to all curves, and this uncertainty has not been included on the horizontal axis. Also, the NROY ratio is set on the vertical axis.

This diagram illustrates several important points. Firstly, at all observation points, the proportion of NROY smoothly increases as uncertainty is incrementally raised, for both the tsunami time series data and the derivative data. This indicates that the functional emulation and the evaluation of distances between functional data conducted through our method have been appropriately performed. Next, this figure can be interpreted to show which observation points are more likely to classify the parameter space as implausible ([McNeall et al. 2016](#)). From the plot for the original curves, at observation point DART 23228, closest to the MSZ, a larger portion of the parameter space is excluded (resulting in a smaller NROY proportion) compared to the most distant point, DART 23011, even when observational errors and model discrepancies are considered significant. This means that assuming identical values of uncertainty at each observation point, the findings indicate that the nearest point exhibits the smallest proportion of the NROY subspace. Therefore, among these four observation points, the data from DART 23228 can be regarded as the most valuable in terms of applying constraints on the parameter space.

For the derivative curves, the order of the proportion excluded for the same value of uncertainty differs from that of the tsunami time series data. This indicates that the differentiated curves, carrying information about the peak and bottom timing of the time series data, contribute differently to align phases. In other words, when the focus is on the velocity of sea surface changes, each observation point impacts the implausibility in a manner different from when sea surface values are targeted. In this method, when estimating uncertainty originating from observational errors and model discrepancies, a conservative approach is taken by adopting the value where 5% is categorized as NROY. Therefore, we use the uncertainty values derived from

Table S1. Square root of the estimated uncertainty (model discrepancy and observational error).

DART	23228	23226	23225	23011
Original curves	29.04	19.55	19.52	14.68
Differentiated curves	215.73	122.87	135.06	124.40

each curve's intersection points with this horizontal line in Figure S7. The square root of these uncertainty values in wave 1 is detailed in Table S1.

The usefulness of history matching is reflected in the NROY proportion. If the assumed uncertainties are overly large, the NROY proportion approaches one and little can be ruled out. Conversely, under defensible uncertainty levels, persistent mismatch between emulator and observations can drive the NROY proportion toward zero. Such outcomes indicate potential misspecification in the simulator, the discrepancy, or the prior input ranges and warrant reassessment.

5. ESTIMATION AT DART LOCATIONS AND IMPLAUSIBILITY ANALYSIS

Figure 4 in the main paper presents the estimated results of wave 1 only at the observation point DART23228, which is closest to the tsunami off the Makran coast. Similarly, the results for wave 1 at other observation points, DART23226, DART23225, and DART23011, are shown in this supplemental material in Figures S8. These figures illustrate the results of (1) one million emulations, (2) functional history matching applied to tsunami time series data at each observation point, and (3) functional history matching results based on sea surface velocity time series data derived from differentiated tsunami time series data combined with the aforementioned functional history matching results for the tsunami time series. These data are derived from an emulator constructed based on an ensemble using the same set of input parameter values obtained through Latin hypercube sampling as mentioned in the main paper. The emulation results based on randomly assigned parameter values shown on the left cannot be said to accurately estimate the worst-case scenario tsunami data represented by a thick black line. This is a natural outcome because the input values are randomly selected. In the middle of the figure, the selected emulation curves that are physically close to the worst-case scenario curve indicate that the functional history matching is effective. Nevertheless, the fact that curves with peaks at different times from the worst-case scenario are also chosen underscores the necessity of employing

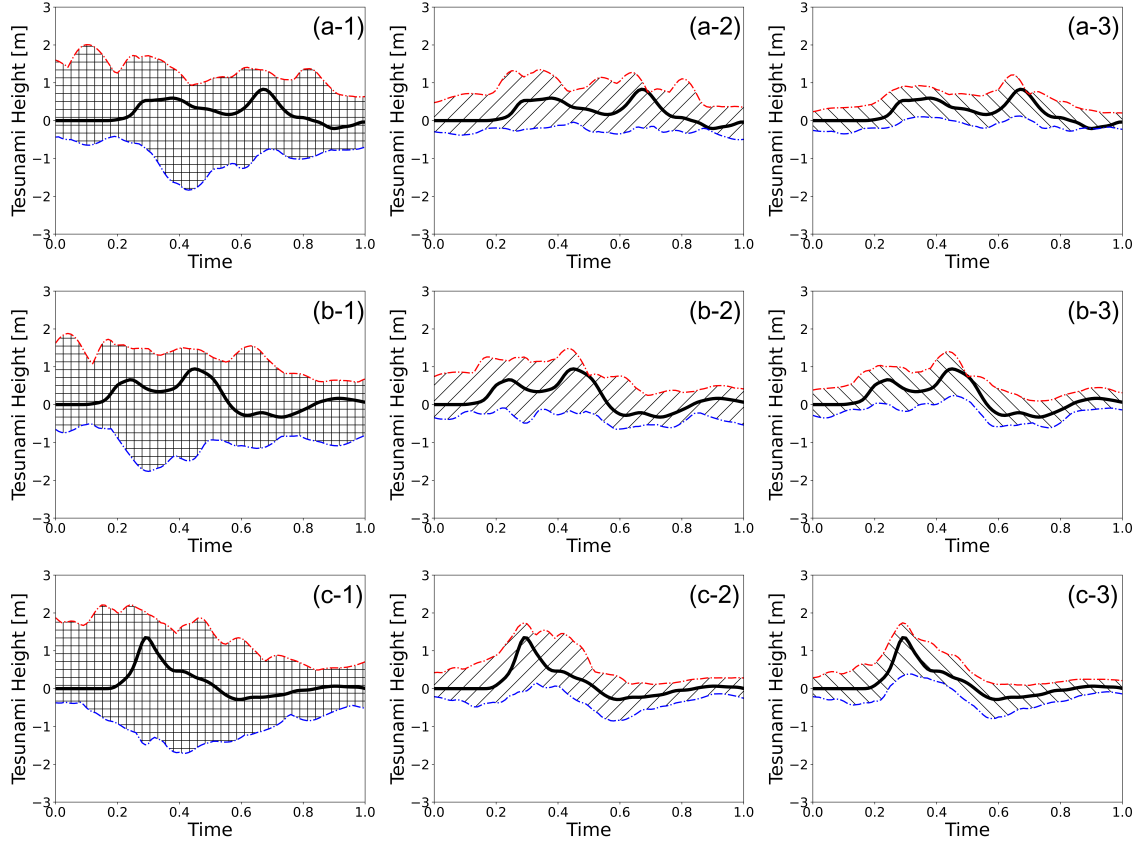


Fig. S8. Emulation Results and Parameter Constraints at the DART 23226, 23225, and 23011 observation Location. Panel (a-1): the results of one million emulations, Panel (a-2): the functional history matching result based on tsunami time series data, and Panel (a-3): the functional history matching result based on tsunami time series data and its derivatives for DART 23226. Regarding DART23225 and DART23011, the figures on the second and third levels are equivalent to those in DART23026.

functional data. This observation is because emulation curves deemed close in physical distance to the worst-case scenario time series do not necessarily share the same positions of peaks and troughs. The results of applying functional history matching to both original tsunami time series data and its derivatives, to incorporate the phase information known as sea surface velocity, are shown on the right. It can be verified that the phases are aligned. These results demonstrate the advantages of functional data analysis by showing that, by taking the information from differentiated curves into account, it is possible to select emulation curves that are physically close to the worst-case scenario time series data and aligned in phase.

Generally, implausibility distribution at different observation points possesses distinct char-

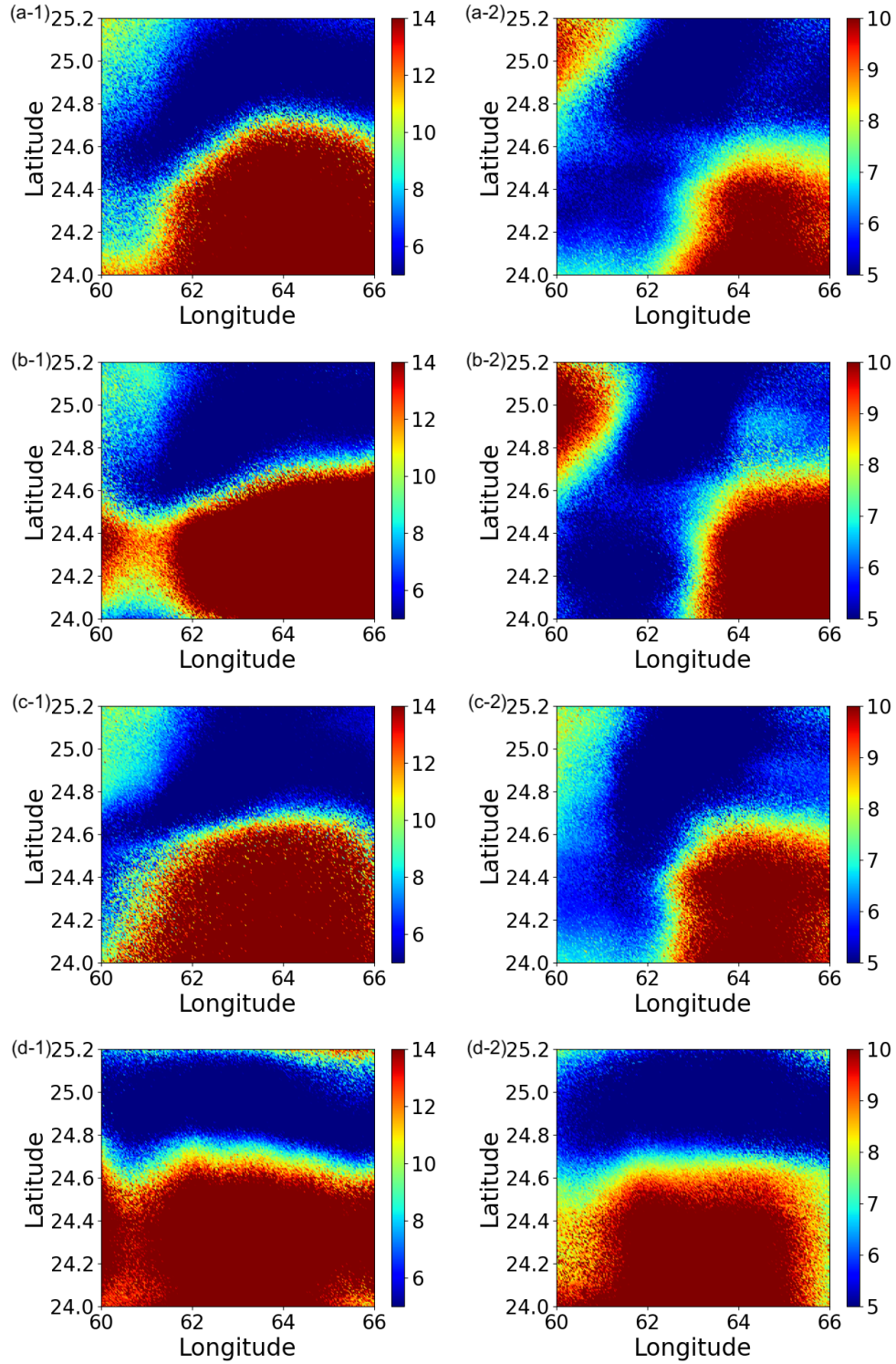


Fig. S9. Distribution of Implausibility for tsunami time series data (left) and the derivative curves (right) at observation points 23228 (a-1, a-2), 23226 (b-1, b-2), 23225 (c-1, c-2), and 23011 (d-1, d-2) during wave 1.

acteristics. To demonstrate this, the distribution of implausibility in wave 1 projected onto a two-dimensional space of longitude and latitude is presented in Figure S9. This figure illustrates, for instance, that the distribution of implausibility calculated from tsunami time series data at the DART23228 station closest to the tsunami source (Panel (a-1)) and implausibility derived from tsunami time series data at the farthest DART23011 station (Panel (d-1)) are different. Furthermore, as demonstrated by the implausibility distributions calculated from the tsunami time series data and their derivative curves, which represent the time series data of sea surface change velocity, significant differences exist at DART23228 and DART23226 as depicted in Panel (a-1) and (a-2), and Panel (b-1) and (b-2), respectively.

6. INVERSE ESTIMATION, FORECASTING AND COMPARISON.

Our functional history matching approach allows for the inverse estimation of the initial tsunami. In this study, a total of 2,381 parameter sets were selected in wave 1, and 497 sets in wave 2. Given the extensive range of longitude direction within the initial parameter space Θ , it is considered challenging to estimate the worst-case scenario tsunami without appropriately selecting a set of parameter values. Figure S10 depicts the inverse estimation of the initial tsunami in the longitude direction at the location where the initial tsunami reaches its highest in the worst-case scenario. As shown in Panel (a), the initial tsunami associated with the set of parameter values constructing the ensemble for the emulator has an average near zero and is bounded by extremely large maximum and minimum values, making it inadequate for accurately estimating the initial tsunami with this data alone. In contrast, the result from wave 1 in Panel (b) shows a reduced range between maximum and minimum values and the estimated average curve closer to the true shape of the initial tsunami. Furthermore, Panel (c) shows that in wave 2 the uncertainty has been reduced and the estimated average shape more closely resembles the worst-case scenario.

Figures S11 displays tsunami forecasting at the observation points 002, 003, and 004 using functional history matching (left) and landmark-based history matching (right). For observation point 002, we examined 90 minutes from 14:30 to 16:00, while for points 003 and 004, it's 120 minutes from 14:00 to 16:00, with the time ranges being transformed to fit within the $[0, 1]$ interval. The forecasting curves using functional history matching are highly accurate with low amplitude. This result means that, although reducing the parameter space does not always contribute to forecasting accuracy, our methodology effectively narrows down the parameter space to facilitate accurate forecasting.

Regarding landmark-based history matching, we constructed an emulator using Gaussian process regression with a Matérn kernel as expressed in Equation S13, targeting four landmarks:

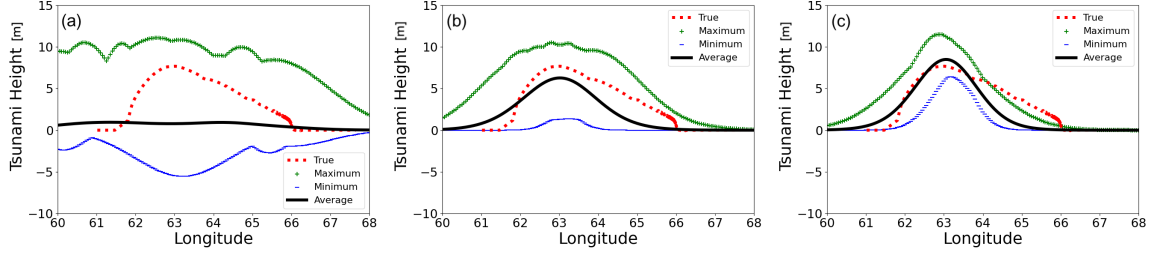


Fig. S10. Inverse estimation of the initial tsunami at the maximum height point in longitude direction. The maximum and minimum values of the selected curves are marked with + and – respectively. A bold black line represents the mean value of the selected curves, while a red dotted line shows the worst-case scenario initial tsunami. Panel (a): Represents the initial tsunami used in 100 JAGURS simulations for constructing the ensemble for the emulator. Panel (b): Results of functional history matching in wave1. Panel (c): Results of functional history matching in wave 2.

the maximum and minimum tsunami heights and the elapsed times to reach these extremes. The emulator was trained using the same simulation ensemble used for functional history matching in wave 1.

$$f(x) \sim \mathcal{GP}(m(x), k(x, x')), \quad (\text{S13})$$

where, x is the input, $f(x)$ is the output corresponding to x , $m(x)$ is the mean function of the Gaussian process, and $k(x, x')$ is the covariance function for any two input points x and x' . In this study, the input x consists of five-dimensional parameters: the longitude and latitude at the midpoint of the tsunami's rise and fall, the standard deviations in the longitude and latitude directions, and the tsunami height. The output is a tsunami value such as the maximum of the tsunami time series data. For this analysis, we assume $m(x) = 0$. Given a set of training data (X, y) , the predicted value $f(x^*)$ at a new input x^* through Gaussian Process Regression is expressed as follows.

$$f(x^*) | X, y, x^* \sim \mathcal{N}(\mu(x^*), \sigma^2(x^*)) \quad (\text{S14})$$

The predicted mean $\mu(x^*)$ and variance σ^2 of the normal distribution that $f(x^*)$ follows are expressed as follows.

$$\mu(x^*) = k(x^*, X) [K + \sigma_n^2 I]^{-1} y \quad (\text{S15})$$

$$\sigma^2(x^*) = k(x^*, x^*) - k(x^*, X) [K + \sigma_n^2 I]^{-1} k(X, x^*) \quad (\text{S16})$$

Here, K denotes the kernel matrix for the training data, σ_n^2 represents the variance of the noise, and I is the identity matrix. Also, this study defines the covariance function using the Matérn

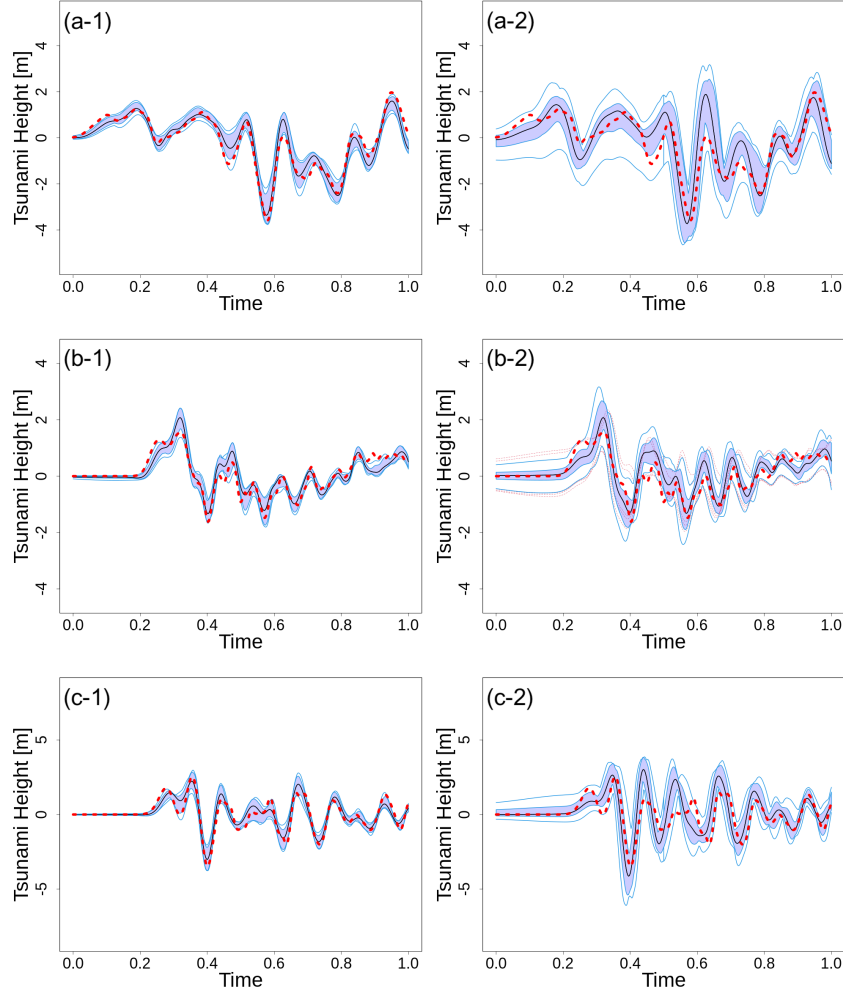


Fig. S11. Tsunami forecasting at Mumbai observation points. Panel (a-1), (b-1), and (c-1) are FHM results in wave 2 at 002, 003, and 004 observation points, respectively. Panel (a-2), (b-2), and (c-2) are landmark-based HM results in wave 2.

kernel, as described below.

$$k(x, x') = \frac{2^{1-\nu}}{\Gamma(\nu)} \left(\frac{\sqrt{2\nu} \|x - x'\|}{l} \right)^\nu K_\nu \left(\frac{\sqrt{2\nu} \|x - x'\|}{l} \right), \quad (\text{S17})$$

where K_ν represents the modified Bessel function of the second kind, Γ denotes the gamma function, and the value of ν is set to 2.5.

Then, we obtained 16 implausibility values $I_1(\theta), \dots, I_{16}(\theta)$ for each θ . Similar to the approach in [Vernon et al. \(2014\)](#), NROY parameter subspace is constructed using the largest implausibility value among 16 calculated measures. After this, the landmark-based history matching method is

Table S2. The number of selected curves based on implausibilities targeting the maximum values, minimum values, and elapsed time to reach them at each DART observation point with landmark-history matching in wave 1.

DART	23228	23226	23225	23011
Max Height	845,408	1,000,000	1,000,000	957,115
Min Height	994,644	983,557	999,836	1,000,000
Max timing	51,454	49,394	110,061	93,096
Min timing	53,685	31,433	89,716	304,202
All	3,601	2,906	16,259	48,289

repeated using the shrunk parameter subspace Θ_1 . It is observed that the maximum heights of the tsunamis near Mumbai are often overestimated, and the amplitude of the estimated tsunami is larger compared to those from our functional history matching approach. In calculating implausibility, we consider only the uncertainty derived from the aforementioned Gaussian process regression as the most extreme assumption. This condition can be considered the assumption that allows for the highest evaluation of implausibility, as evidenced by the reduction in implausibility values when additional uncertainties such as observational errors or model discrepancy are incorporated, thus enabling the greatest exclusion of parameter subspace.

Nevertheless, the outcomes of performing history matching independently for maximum and minimum values, and their arrival times at each DART observation site, as shown in Table S2, did not function efficiently. Despite considering only the uncertainty originating from Gaussian process regression, which was thought to be extremely advantageous for reducing the NROY subspace, the history matching for discrete data did not function properly. This indicates that using only these specific observation points for the time series data is insufficient.

7. VIRTUAL OBSERVATION POINT

By placing a hypothetical observation point at the location indicated by the black circle in Figure S1, we examine the changes that occur compared to functional history matching conducted only with the existing four DART observation points. This aims to understand the impact of constructing the NROY parameter subspace when adding an observation point on the opposite

side, as opposed to having all observation points in the same direction from the tsunami source. Figure S12 includes the results of the initial tsunami inverse-estimation at the locations recording the maximum and minimum tsunami heights in the worst-case scenario, at (63.017, 24.366) and (63.623, 25.311) respectively. Comparisons between Panel (a) and (b), as well as Panel (c) and (d), clearly demonstrate a reduction in the NROY subspace in low-longitude regions, indicating that even a single virtual observation point can be highly effective.

To assess the specific effects on the NROY parameter subspace shrinkage caused by this virtual observation point, Figure S13 presents violin plots showing the non-implausible regions for each parameter, where it is evident that there is a significant restriction in the longitude and the tsunami height. It can also be seen that there is a minor contraction in the S_{xx} direction. One possible reason for observing such a phenomenon is that tsunamis located at low longitude need to be exceptionally large to replicate the worst-case scenarios at the four DART observation points. However, it is hypothesized that the virtual observation point on the opposite side of the DART points has eliminated such large tsunamis.

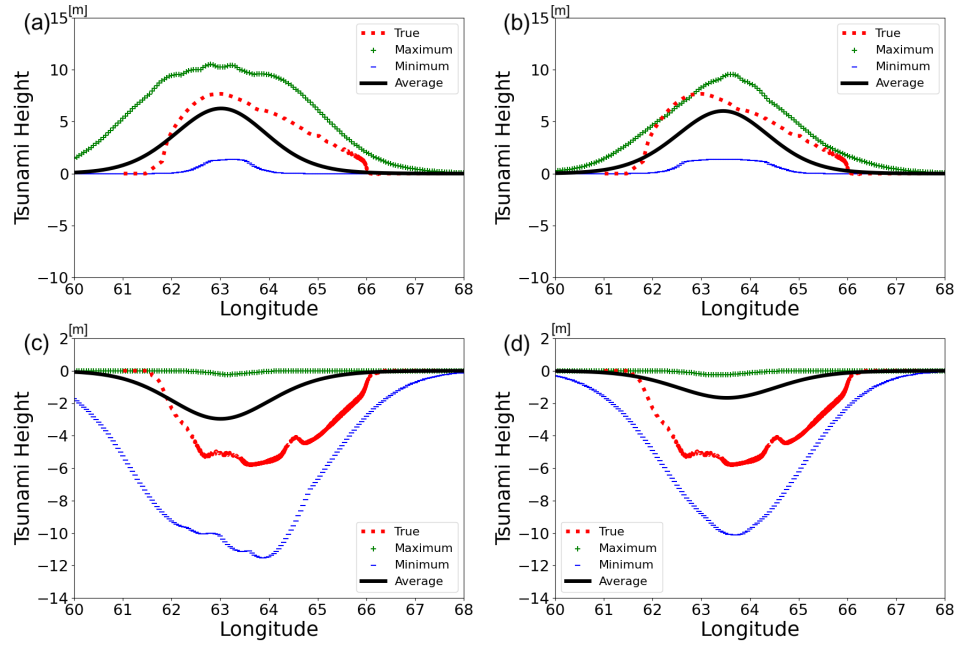


Fig. S12. Comparison of the estimation of initial tsunami (longitude direction) using only four DART observation points, Panel (a) and (c), versus adding a virtual observation point, Panel (b) and (d), in wave 1. Panel (a) and (b): The initial tsunami estimation at the location of the highest tsunami height under the worst-case scenario. Panel (c) and (d): The initial tsunami estimation at the location of the lowest tsunami height under the worst-case scenario.

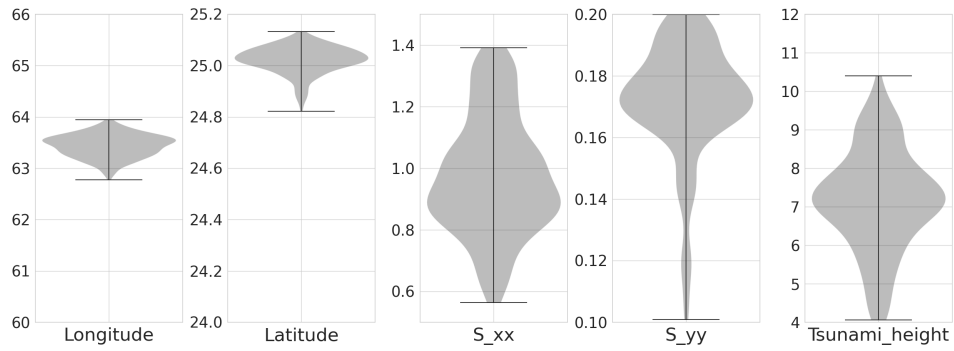


Fig. S13. Violin plots with an additional virtual observation point added to the four DART observation points in wave 1.

REFERENCES

- Alt, H. & Godau, M. (1995), 'Computing the fréchet distance between two polygonal curves', *International Journal of Computational Geometry & Applications* 5(01n02), 75–91.
- Arriaga, R. I., Rutter, D., Cakmak, M. & Vempala, S. S. (2015), 'Visual categorization with random projection', *Neural computation* 27(10), 2132–2147.
- Baba, T., Allgeyer, S., Hossen, J., Cummins, P. R., Tsushima, H., Imai, K., Yamashita, K. & Kato, T. (2017), 'Accurate numerical simulation of the far-field tsunami caused by the 2011 tohoku earthquake, including the effects of boussinesq dispersion, seawater density stratification, elastic loading, and gravitational potential change', *Ocean Modelling* 111, 46–54.
- Baba, T., Takahashi, N., Kaneda, Y., Ando, K., Matsuoka, D. & Kato, T. (2015), 'Parallel implementation of dispersive tsunami wave modeling with a nesting algorithm for the 2011 tohoku tsunami', *Pure and Applied Geophysics* 172, 3455–3472.
- Berlinet, A. & Thomas-Agnan, C. (2011), *Reproducing kernel Hilbert spaces in probability and statistics*, Springer Science & Business Media.
- Brankovic, M., Buchin, K., Klaren, K., Nusser, A., Popov, A. & Wong, S. (2020), (k, l)-medians clustering of trajectories using continuous dynamic time warping, in 'Proceedings of the 28th International Conference on Advances in Geographic Information Systems', pp. 99–110.
- Brown, R. (1828), 'Xxvii. a brief account of microscopical observations made in the months of june, july and august 1827, on the particles contained in the pollen of plants; and on the general existence of active molecules in organic and inorganic bodies', *The philosophical magazine* 4(21), 161–173.
- Ferreira, L. & Hitchcock, D. B. (2009), 'A comparison of hierarchical methods for clustering functional data', *Communications in Statistics-Simulation and Computation* 38(9), 1925–1949.
- Geppert, L. N., Ickstadt, K., Munteanu, A., Quedenfeld, J. & Sohler, C. (2017), 'Random projections for bayesian regression', *Statistics and Computing* 27, 79–101.
- Gopinathan, D., Heidarzadeh, M. & Guillas, S. (2021), 'Probabilistic quantification of tsunami current hazard using statistical emulation', *Proceedings of the Royal Society A* 477(2250), 20210180.
- Hall, P., Müller, H.-G. & Wang, J.-L. (2006), 'Properties of principal component methods for functional and longitudinal data analysis', *The Annals of Statistics* 34(3), 1493 – 1517.
URL: <https://doi.org/10.1214/0090536060000000272>
- Hitchcock, D. B., Casella, G. & Booth, J. G. (2006), 'Improved estimation of dissimilarities by presmoothing functional data', *Journal of the American Statistical Association* 101(473), 211–222.
- James, G. M. & Sugar, C. A. (2003), 'Clustering for sparsely sampled functional data', *Journal of the American Statistical Association* 98(462), 397–408.
- Karhunen, K. (1947), 'Under lineare methoden in der wahr scheinlichkeitsrechnung', *Annales Academiae Scientiarum Fennicae Series A1: Mathematica Physica* 47.
- Loeve, M. (1948), 'Fonctions aleatoires du second ordre', *Processus stochastique et mouvement*

- Brownien* pp. 366–420.
- Maillard, O. & Munos, R. (2012), ‘Linear regression with random projections’, *Journal of Machine Learning Research* **13**(1), 2735–2772.
- Mandelbrot, B. B. & Van Ness, J. W. (1968), ‘Fractional brownian motions, fractional noises and applications’, *SIAM review* **10**(4), 422–437.
- Marron, J. S., Ramsay, J. O., Sangalli, L. M. & Srivastava, A. (2015), ‘Functional data analysis of amplitude and phase variation’, *Statistical Science* pp. 468–484.
- McNeill, D., Williams, J., Booth, B., Betts, R., Challenor, P., Wiltshire, A. & Sexton, D. (2016), ‘The impact of structural error on parameter constraint in a climate model’, *Earth System Dynamics* **7**(4), 917–935.
- Ramsay, J. O. & Silverman, B. W. (2005), *Fitting differential equations to functional data: Principal differential analysis*, Springer.
- Rougier, J. (2008), ‘Efficient emulators for multivariate deterministic functions’, *Journal of Computational and Graphical Statistics* **17**(4), 827–843.
- Sakoe, H. & Chiba, S. (1978), ‘Dynamic programming algorithm optimization for spoken word recognition’, *IEEE transactions on acoustics, speech, and signal processing* **26**(1), 43–49.
- Tasoulis, S., Cheng, L., Välimäki, N., Croucher, N. J., Harris, S. R., Hanage, W. P., Roos, T. & Corander, J. (2014), Random projection based clustering for population genomics, in ‘2014 IEEE international conference on big data (big data)’, IEEE, pp. 675–682.
- Tokushige, S., Inada, K. & Yadohisa, H. (2003), ‘8. functional data analysis dissimilarity and related methods for functional data’, *Journal of the Japanese Society of Computational Statistics* **15**(2), 319–326.
- Uhlenbeck, G. E. & Ornstein, L. S. (1930), ‘On the theory of the brownian motion’, *Physical review* **36**(5), 823.
- Vernon, I., Goldstein, M. & Bower, R. (2014), ‘Galaxy formation: Bayesian history matching for the observable universe’, *Statistical science* pp. 81–90.
- Xie, H., Li, J., Zhang, Q. & Wang, Y. (2016), ‘Comparison among dimensionality reduction techniques based on random projection for cancer classification’, *Computational biology and chemistry* **65**, 165–172.
- Zhao, K., Alavi, A., Wiliem, A. & Lovell, B. C. (2016), ‘Efficient clustering on riemannian manifolds: A kernelised random projection approach’, *Pattern Recognition* **51**, 333–345.